Chapter 4
Forced Convection

The fundamental question in heat transfer engineering is to determine the relationship between the heat transfer rate and the driving temperature difference. In nature, many saturated porous media interact thermally with one another and with solid surfaces that confine them or are embedded in them. In this chapter we analyze the basic heat transfer question by looking only at *forced convection* situations, in which the fluid flow is caused (forced) by an external agent unrelated to the heating effect. First we discuss the results that have been developed based on the Darcy flow model and later we address work on the non-Darcy effects. We end this chapter with a review of current engineering applications of the method of forced convection through porous media. Some fundamental aspects of the subject have been discussed by Lage and Narasimhan (2000) and the topic has been reviewed by Lauriat and Ghafir (2000) and Zheng et al. (2012).

4.1 Plane Wall with Prescribed Temperature

Perhaps the simplest and most common heat transfer arrangement is the flow parallel to a flat surface that borders the fluid-saturated porous medium. With reference to the two-dimensional geometry defined in Fig. 4.1, we recognize the equations governing the conservation of mass, momentum (Darcy flow), and energy in the flow region of thickness δ_T:

$$\frac{\partial u}{\partial x}+\frac{\partial v}{\partial y}=0, \tag{4.1}$$

$$u=-\frac{K}{\mu}\frac{\partial P}{\partial x}, \quad v=-\frac{K}{\mu}\frac{\partial P}{\partial y}, \tag{4.2}$$

D.A. Nield, A. Bejan, *Convection in Porous Media*,
DOI 10.1007/978-3-319-49562-0_4

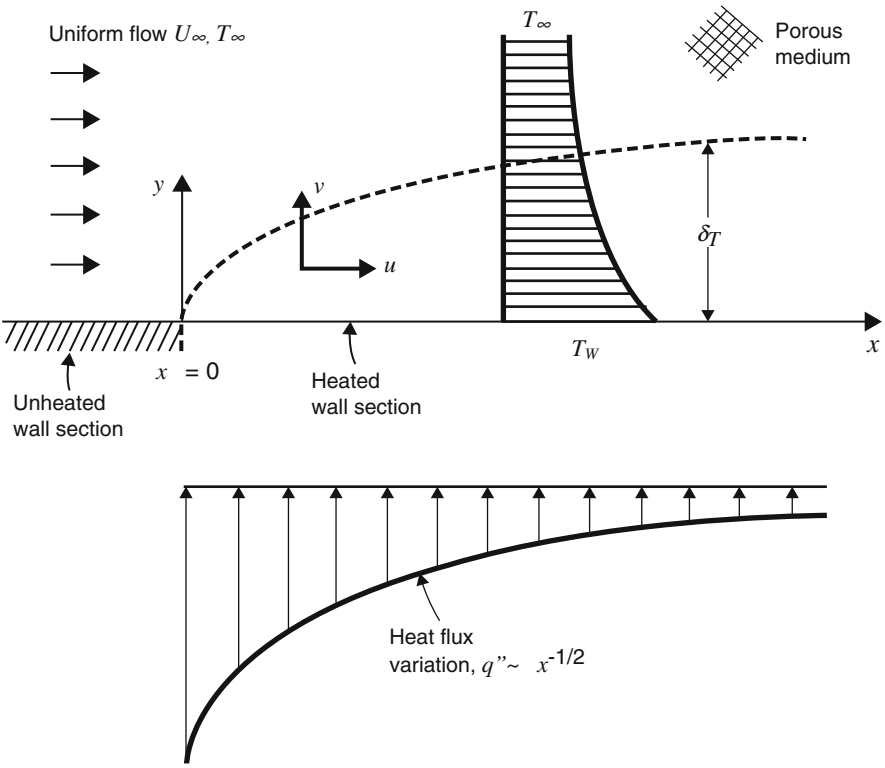

Fig. 4.1 Parallel flow near an isothermal wall (Bejan 1984)

$$u\,\frac{\partial T}{\partial x}+v\,\frac{\partial T}{\partial y}=\alpha_{\mathrm{m}}\,\frac{\partial^2 T}{\partial y^2}. \tag{4.3}$$

Note the boundary layer-approximated right-hand side of Eq. (4.3), which is based on the assumption that the region of thickness δ_T and length x is slender ($\delta_T \ll x$). The fluid mechanics part of the problem statement [namely, Eqs. (4.1) and (4.2)] is satisfied by the uniform parallel flow

$$u = U, \quad v = 0, \tag{4.4}$$

The constant pressure gradient that drives this flow ($-dP/dx = \mu U_\infty/K$) is assumed known.

The heat transfer rate between the surface at temperature T_w and the saturated porous medium at far-field temperature T_∞ can be determined in several ways. The scale analysis begins with writing $\Delta T = T_w - T_\infty$, so that the order-of-magnitude counterpart of Eq. (4.3) becomes

$$U_\infty \frac{\Delta T}{x} \sim \alpha_m \frac{\Delta T}{\delta_T^2}. \tag{4.5}$$

From this we can determine the thickness of the thermal boundary layer

$$\delta_T \sim x \mathrm{Pe}_x^{-1/2}, \tag{4.6}$$

in which Pe_x is the Péclet number based on U_∞ and x:

$$\mathrm{Pe}_x = \frac{U_\infty x}{\alpha_m}. \tag{4.7}$$

For the local heat flux q'' we note the scale $q'' \sim k_m \, \Delta T/\delta_T$, or the corresponding local Nusselt number

$$\mathrm{Nu}_x = \frac{q''}{\Delta T} \frac{x}{k_m} \sim \mathrm{Pe}_x^{1/2}. \tag{4.8}$$

Figure 4.1 qualitatively illustrates the main characteristics of the heat transfer region, namely, the boundary layer thickness that increases as $x^{1/2}$ and the heat flux that decays as $x^{-1/2}$. The exact analytical solution for the same problem can be derived in closed form by introducing the similarity variables recommended by the scale analysis presented above:

$$\eta = \frac{y}{x} \mathrm{Pe}_x^{1/2}, \quad \theta(\eta) = \frac{T - T_w}{T_\infty - T_w}. \tag{4.9}$$

In this notation, the energy equation (4.3) and the boundary conditions of Fig. 4.1 become

$$\theta'' + \frac{1}{2} \eta \theta' = 0, \tag{4.10}$$

$$\theta(0) = 0, \quad \theta(\infty) = 1. \tag{4.11}$$

Equation (4.10) can be integrated by separation of variables, and the resulting expressions for the similarity temperature profile and the surface heat flux are (Bejan 1984):

$$\theta = \mathrm{erf}\left(\frac{\eta}{2}\right), \tag{4.12}$$

$$\mathrm{Nu}_x = \frac{q''}{T_w - T_\infty} \frac{x}{k_m} = 0.564 \mathrm{Pe}_x^{1/2}, \tag{4.13}$$

The overall Nusselt number based on the heat flux $\bar{q}''$ averaged from $x = 0$ to a given plate length $x = L$ is

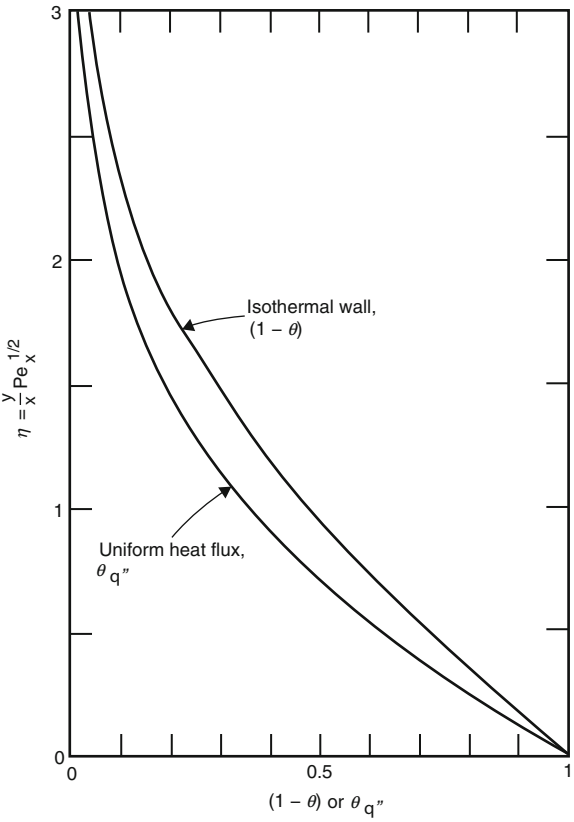

Fig. 4.2 The temperature distributions in a forced parallel flow near walls with constant temperature and constant heat flux (Bejan 1984)

$$\overline{\mathrm{Nu}_\mathrm{L}} = \frac{\overline{q''}}{T_\mathrm{w} - T}\frac{L}{k_\mathrm{m}} = 1.128\,\mathrm{Pe}_\mathrm{L}^{1/2}. \tag{4.14}$$

Cheng (1977c) found the same Nu_x result by integrating numerically the equivalent of Eqs. (4.10) and (4.11) for a wider class of problems. The similarity temperature profile (4.12) has been plotted as $(1 - \theta)$ versus η in Fig. 4.2. The effect of viscous dissipation has been included in the analysis by Magyari et al. (2003b). An experimental study of forced convection over a horizontal plate in a porous medium was reported by Afifi and Berbish (1999). A finite-element study was made by Krishna et al. (1999). Magyari et al. (2001a) presented some exact analytical solutions for forced convection past a plane or axisymmetric body having a power-law surface distribution. Li and Tu (2008) and Li et al. (2009) obtained an integral solution for forced convection over an isothermal plate.

4.2 Plane Wall with Constant Heat Flux

When the surface heat flux q'' is independent of x the temperature difference $T_w - T_\infty$ increases as x in the downstream direction. This can be seen by combining the heat flux scale $q'' \sim k_m(T_w - T_\infty)/\delta_T$ with the δ_T scale (4.6), which applies to the constant q'' configuration as well. The similarity solution for the temperature distribution along and near the $y = 0$ surface was determined numerically by Bejan (1984),

$$T(x,y) - T_\infty = \frac{q''/k_m}{\left(-d\theta_{q''}/d\eta\right)_{\eta=0}} \left(\frac{\alpha_m x}{U}\right)^{1/2} \theta_{q''}(\eta), \tag{4.15}$$

in which $\theta_{q''}(\eta)$ is the similarity temperature profile displayed in Fig. 4.2. The similarity variable η is defined on the ordinate of the figure. Since the calculated slope of the $\theta_{q''}$ profile at the wall is $(-d\theta_{q''}/d\eta)_{\eta=0} = 0.886$, the inverse of the local temperature difference can be nondimensionalized as the local Nusselt number

$$\mathrm{Nu}_x = \frac{q''}{T_w(x) - T} \frac{x}{k_m} = 0.886\,\mathrm{Pe}_x^{1/2}. \tag{4.16}$$

The overall Nusselt number that is based on the average wall temperature $\bar{T}_w$ (specifically, the temperature averaged from $x = 0$ to $x = L$) is

$$\overline{\mathrm{Nu}_L} = \frac{q''}{\bar{T}_w - T} \frac{L}{k_m} = 1.329\,\mathrm{Pe}_L^{1/2}. \tag{4.17}$$

We use this opportunity to communicate the exact solution for the problem of heat transfer from an embedded wall with uniform heat flux. The closed-form analytical alternative to the numerical solution (4.15) shown in Fig. 4.2 is

$$\frac{T(x,y) - T_\infty}{q'' x/k_m} \mathrm{Pe}_x^{1/2} = 2\pi^{-1/2} \exp\left(-\frac{\eta^2}{4}\right) - \eta\ \mathrm{erfc}\left(\frac{\eta}{2}\right). \tag{4.18}$$

The right-hand side of Eq. (4.18) now replaces the function $\theta_{q''}/(-d\theta_{q''}/d\eta)_{\eta=0}$ used earlier in (4.15). This exact solution also reveals the exact values of the numerical coefficients that appear in Eqs. (4.16) and (4.17), namely $0.886 = \pi^{1/2}/2$ and $1.329 = (3/4)\pi^{1/2}$.

It is worth reviewing the Nusselt number results (4.13), (4.16), and (4.17), in order to rediscover the order-of-magnitude trend anticipated in Eq. (4.8). All these results are valid if $\delta_T \ll x$, i.e., when the Péclet number is sufficiently large so that $\mathrm{Pe}_x^{1/2} \gg 1$. The effect of variation of viscosity with temperature was studied by Ramirez and Saez (1990) and Ling and Dybbs (1992).

Mahgoub (2013) reported experimental results for the constant flux case.

4.3 Sphere and Cylinder: Boundary Layers

A conceptually similar forced convection boundary layer develops over any other body that is imbedded in a porous medium with uniform flow. Sketched in Fig. 4.3 is the thermal boundary layer region around a sphere, or around a circular cylinder that is perpendicular to the uniform flow with volume-averaged velocity u. The sphere or cylinder radius is r_0 and the surface temperature is T_w.

The distributions of heat flux around the sphere and cylinder were determined by Cheng (1982), who assumed that the flow obeys Darcy's law. With reference to the angular coordinate θ defined in Fig. 4.3, Cheng obtained the following expressions for the local peripheral Nusselt number:

Sphere:

$$\mathrm{Nu}_\theta = 0.564\left(\frac{ur_0\theta}{\alpha_m}\right)^{1/2}\left(\frac{3}{2}\theta\right)^{1/2}\sin^2\theta\left(\frac{1}{3}\cos^3\theta - \cos\theta + \frac{2}{3}\right)^{1/2}. \tag{4.19}$$

Cylinder:

$$\mathrm{Nu}_\theta = 0.564\left(\frac{ur_0\theta}{\alpha_m}\right)^{1/2}(2\theta)^{1/2}\sin\theta(1-\cos\theta)^{1/2}. \tag{4.20}$$

Worth noting in these expressions is the Péclet number based on the swept arc $r_0\theta$, namely $\mathrm{Pe}_\theta = u\, r_0\theta/\alpha_m$. The local Nusselt number is defined as

$$\mathrm{Nu}_\theta = \frac{q''}{T_w - T_\infty}\frac{r_0\theta}{k_m}. \tag{4.21}$$

The variation of the local heat flux over the cylinder or sphere circumference is illustrated in terms of $[q''r_0/k_m(T_w - T_\infty)](ur_0/\alpha_m)^{-1/2}$ versus θ in Fig. 4.4.

Equations (4.19) and (4.20) are valid when the boundary layers are distinct (thin), i.e., when the boundary layer thickness $r_0\mathrm{Pe}_\theta^{1/2}$ is smaller than the radius r_0. This requirement can also be written as $\mathrm{Pe}_\theta^{1/2} \gg 1$, or $\mathrm{Nu}_\theta \gg 1$.

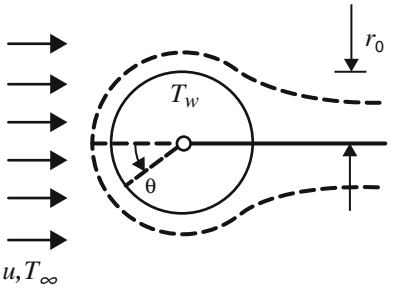

Fig. 4.3 The forced-convection thermal boundary layer around a sphere or perpendicular cylinder embedded in a porous medium

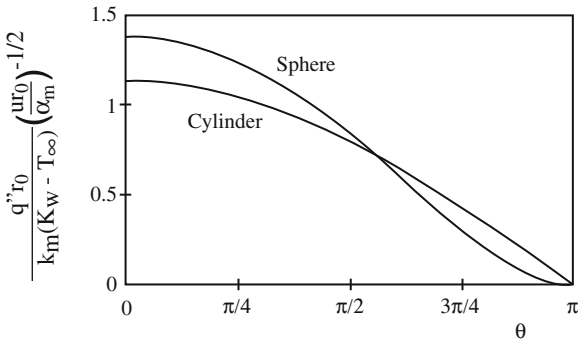

Fig. 4.4 The distribution of heat flux over a cylinder or sphere with forced-convection boundary layer

The conceptual similarity between the thermal boundary layers of the cylinder and the sphere (Fig. 4.3) and that of the flat wall (Fig. 4.1) is illustrated further by the following attempt to correlate the heat transfer results for these three configurations. The heat flux averaged over the area of the cylinder and sphere, $\overline{q''}$, can be calculated by averaging the local heat flux q'' expressed by Eqs. (4.19)–(4.21). We have done this on this occasion, and the results are:

$$\text{Sphere}: \qquad \overline{\text{Nu}_D} = 1.128\,\text{Pe}_D^{1/2}, \tag{4.22}$$

$$\text{Cylinder}: \qquad \overline{\text{Nu}_D} = 1.015\,\text{Pe}_D^{1/2}. \tag{4.23}$$

In these expressions, the Nusselt and Péclet numbers are based on the diameter $D = 2r_0$,

$$\overline{\text{Nu}_D} = \frac{\overline{q''}}{T_w - T}\frac{D}{k_m}, \qquad \text{Pe}_D = \frac{uD}{\alpha_m}. \tag{4.24}$$

Remarkable at this stage is the similarity between the $\overline{\text{Nu}_D}$ expressions (4.22) and (4.23), and between this set and the corresponding $\overline{\text{Nu}_L}$ formula for the isothermal flat wall, Eq. (4.14). The correlation of these three results is very successful because in each case the length scale used in the definition of the overall Nusselt number and the Péclet number is the dimension that is aligned with the direction of flow, the diameter in Fig. 4.3, and the length L in Fig. 4.1.

In an earlier attempt to correlate the overall heat transfer rates for these three configurations, as length scale we used Lienhard's (1973) "swept" length l, namely $l = L$ for the flat wall and $l = \pi r_0$ for the cylinder and sphere. We found that this length scale does not work nearly as well; in other words, the resulting $\overline{\text{Nu}_l} \sim \text{Pe}_l$ expressions change appreciably from one configuration to the next. In defense of Lienhard's length scale, however, it must be said that it was originally proposed for natural convection boundary layers, not forced convection.

The heat transfer by forced convection from a cylinder with elliptic cross section to the surrounding saturated porous medium was analyzed by Kimura (1988a). This

geometry bridges the gap between the circular cylinder and the plane wall discussed in Sect. 4.1. The elliptic cylinder in cross flow is in itself relevant as a model for the interaction between a uniform flow and a circular cylinder that is not perpendicular to the flow direction. The extreme case in which the circular cylinder is parallel to the flow direction was also analyzed by Kimura (1988b). A circular cylinder with constant heat flux was studied by Kimura and Yoneysa (1992). A problem involving a magnetic field was treated by Ghadi et al. (2012).

Murty et al. (1990) investigated non-Darcy effects and found that heat transfer from a cylinder was only weakly dependent on Darcy and Forchheimer numbers for $\mathrm{Da} < 10^{-4}$, $\mathrm{Re} < 200$.

An experimental study of heat transfer from a cylinder embedded in a bed of spherical particles, with cross flow of air, was made by Nasr et al. (1994). Agreement with theory based on Darcy's law and boundary layer approximations was found to be moderately successful in predicting the data, but improved correlations were obtained with an equation modified to better account for particle diameter and conductivity variations. A similar experimental study was made by Afifi and Berbish (1998).

For axial flow past a cylinder, an experimental study, with water and glass beads, was carried out by Kimura and Nigorinuma (1991). Their experimental results agreed well with an analysis, similar to that for the flat plate problem but with the curvature taken into account. Three exactly solvable cases with axial flow were studied by Magyari (2013b).

Heat transfer from a large sphere imbedded in a bed of spherical glass beads was studied experimentally by Tung and Dhir (1993). They concluded that the total rate of heat transfer could be predicted from the equation

$$\mathrm{Nu} = \mathrm{Nu}_{\mathrm{conduction}} + \mathrm{Nu}_{\mathrm{radiation}} + \left(\mathrm{Nu}_{\mathrm{natural}}^3 + \mathrm{Nu}_{\mathrm{forced}}^3\right)^{1/3}, \tag{4.25}$$

where

$$\mathrm{Nu}_{\mathrm{forced}} = 0.29\,\mathrm{Re}^{0.8}\mathrm{Pr}^{1/2}, \quad 0.7 \leq \mathrm{Pr} \leq 5, \mathrm{Re} \leq 2400. \tag{4.26}$$

where Re is the Reynolds number based on the diameter of the large sphere.

Asymptotic solutions, valid for high or low (respectively) Pe, for the case of a sphere with either prescribed temperature or prescribed flux, were obtained by Romero (1994, 1995a). Analytical solutions for large Péclet numbers for flow about a cylinder or sphere were reported by Pop and Yan (1998). Numerical simulation of forced convection past a parabolic cylinder was carried out by Haddad et al. (2002). MHD and viscous dissipation effects for flow past a cylinder were studied by El-Amin (2003a). Further analysis of forced convection from a circular cylinder was reported by Al-Sumaily et al. (2012a,b), who studied the effect of local thermal nonequilibrium. Khadrawi et al. (2005a) studied non-Darcy convection past a wedge or cone.

Juncu (2014) studied the effect of permeability on unsteady conjugate convection from a sphere.

4.4 Point Source and Line Source: Thermal Wakes

In the region downstream from the hot sphere or cylinder of Fig. 4.3, the heated fluid forms a thermal wake whose thickness increases as $x^{1/2}$. This behavior is illustrated in Fig. 4.5, in which x measures the distance downstream from the heat source. Seen from the distant wake region, the imbedded sphere appears as a point source (Fig. 4.5, left), while the cylinder perpendicular to the uniform flow (u, T_∞) looks like a line source (Fig. 4.5, right).

Consider the two-dimensional frame attached to the line source q' in Fig. 4.5, right. The temperature distribution in the wake region, $T(x,y)$, must satisfy the energy conservation equation

$$u\,\frac{\partial T}{\partial x} = \alpha_{\mathrm{m}}\,\frac{\partial^2 T}{\partial y^2}, \tag{4.27}$$

the boundary conditions $T \to T_\infty$ as $y \to \pm\infty$, and the integral condition

$$q' = \int_{-\infty}^{\infty} (\rho c_{\mathrm{P}})_{\mathrm{f}} u (T - T_\infty)\, dy. \tag{4.28}$$

Restated in terms of the similarity variable η and the similarity temperature profile θ,

$$\eta = \frac{y}{x}\mathrm{Pe}_{\mathrm{x}}^{1/2}, \quad \theta(\eta) = \frac{T - T_\infty}{q'/k_{\mathrm{m}}}\mathrm{Pe}_{\mathrm{x}}^{1/2}, \tag{4.29}$$

in which $\mathrm{Pe}_{\mathrm{x}} = ux/\alpha_{\mathrm{m}}$, the problem statement becomes

$$-\frac{1}{2}(\theta + \eta\theta') = \theta'', \tag{4.30}$$

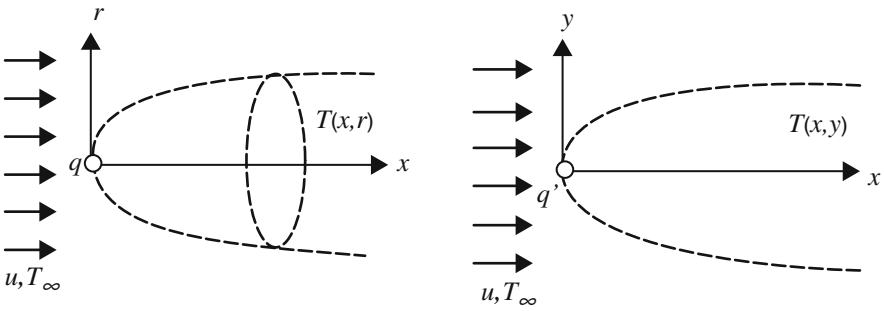

Fig. 4.5 The thermal wakes behind a point source (*left*), and behind a line source perpendicular to the uniform flow (*right*)

$$\theta \to 0 \quad \text{as} \quad \eta \to \pm\infty \tag{4.31}$$

$$\int_{-\infty}^{\infty} \theta d\eta = 1. \tag{4.32}$$

The solution can be determined analytically,

$$\theta = \frac{1}{2\pi^{1/2}} \exp\left(-\frac{\eta^2}{4}\right). \tag{4.33}$$

In terms of the physical variables, the solution is

$$T - T_\infty = 0.282 \frac{q'}{k_\mathrm{m}} \left(\frac{\alpha_\mathrm{m}}{ux}\right)^{1/2} \exp\left(-\frac{uy^2}{4\alpha_\mathrm{m} x}\right). \tag{4.34}$$

In conclusion, the wake temperature distribution has a Gaussian profile in y. The width of the wake increases as $x^{1/2}$, while the temperature excess on the centerline $[T(x,0) - T_\infty]$ decreases as $x^{-1/2}$.

The corresponding solution for the temperature distribution $T(x,r)$ in the round wake behind the point source q of Fig. 4.5, left, is

$$T - T_\infty = \frac{q}{4\pi k_\mathrm{m} x} \exp\left(-\frac{ur^2}{4\alpha_\mathrm{m} x}\right), \tag{4.35}$$

In this case, the excess temperature on the wake centerline decreases as x^{-1}, that is more rapidly than on the centerline of the two-dimensional wake.

Both solutions, Eqs. (4.34) and (4.35), are valid when the wake region is slender, in other words when $\mathrm{Pe}_x \gg 1$. When this Péclet number condition is not satisfied, the temperature field around the source is dominated by the effect of thermal diffusion, not convection. In such cases, the effect of the heat source is felt in all directions, not only downstream.

In the limit where the flow (u, T_∞) is so slow that the convection effect can be neglected, the temperature distribution can be derived by the classic methods of pure conduction. A steady-state temperature field can exist only around the point source,

$$T(r) - T_\infty = \frac{q}{4\pi k_\mathrm{m} r}. \tag{4.36}$$

The pure conduction temperature distribution around the line source remains time dependent (all the temperatures rise; e.g., Bejan 1993, p. 181). When the time t is sufficiently long so that $(x^2 + y^2)/(4\alpha_\mathrm{m} t) \ll 1$, the excess temperature around the line source is well approximated by

$$T(r,t) - T_\infty \cong \frac{q'}{4\pi k_\mathrm{m}} \left[\ln\left(\frac{4\alpha_\mathrm{m} t}{\sigma r^2}\right) - 0.5772\right]. \tag{4.37}$$

In this expression, r^2 is shorthand for $(x^2 + y^2)$. We will return to the subject of buried heat sources in Sects. 5.10 and 5.11.

4.5 Confined Flow

We now consider the forced convection heat transfer in a channel or duct packed with a porous material (Fig. 4.6). In the Darcy flow regime the longitudinal volume-averaged velocity u is uniform over the channel cross section. For this reason, when the temperature field is fully developed, the relationship between the wall heat flux q'' and the local temperature difference $(T_w - T_b)$ is analogous to the formula for fully developed heat transfer to "slug flow" through a channel without a porous matrix. The temperature T_b is the mean or bulk temperature of the stream that flows through the channel (e.g., Bejan 1984, p. 83). The T_b definition for slug flow reduces to

$$T_b = \frac{1}{A}\int_A T\,dA, \tag{4.38}$$

in which A is the area of the channel cross section.

In cases where the confining wall is a tube with the internal diameter D, the relation for fully developed heat transfer can be expressed as a constant Nusselt number (Rohsenow and Choi 1961):

$$\mathrm{Nu}_D = \frac{q''(x)}{T_w - T_b(x)}\frac{D}{k_m} = 5.78 \quad (\text{tube}, T_w = \text{constant}), \tag{4.39}$$

$$\mathrm{Nu}_D = \frac{q''}{T_w(x) - T_b(x)}\frac{D}{k_m} = 8 \quad \left(\text{tube}, q'' = \text{constant}\right). \tag{4.40}$$

When the porous matrix is sandwiched between two parallel plates with the spacing D, the corresponding Nusselt numbers are (Rohsenow and Hartnett 1973)

$$\mathrm{Nu}_D = \frac{q''(x)}{T_w - T_b(x)}\frac{D}{k_m} = 4.93 \quad (\text{parallel plates}, T_w = \text{constant}), \tag{4.41}$$

$$\mathrm{Nu}_D = \frac{q''}{T_w(x) - T_b(x)}\frac{D}{k_m} = 6 \quad \left(\text{parallel plates}, \ q'' = \text{constant}\right). \tag{4.42}$$

The forced convection results [Eqs. (4.39)–(4.42)] are valid when the temperature profile across the channel is fully developed, i.e., sufficiently far from the

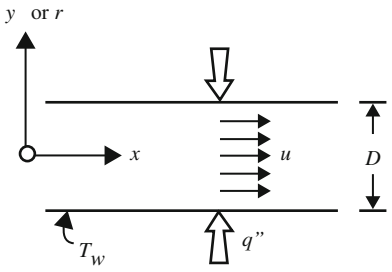

Fig. 4.6 Heat transfer to the Darcy flow forced through the porous medium confined by the walls of a channel or duct

entrance $x = 0$ (Fig. 4.6). The entrance length, or the length needed for the temperature profile to become fully developed, can be estimated by recalling from Eq. (4.6) that the thermal boundary layer thickness scales as $(\alpha_m x/u)^{1/2}$. By setting $(\alpha_m x/u)^{1/2} \sim D$ we obtain the thermal entrance length $x_T \sim D^2 u/\alpha_m$. Inside the entrance region $0 < x < x_T$, the heat transfer is impeded by the forced convection thermal boundary layers that line the channel walls, and can be calculated approximately with the formulas presented in Sects. 4.1 and 4.2.

One important application of the results for a channel packed with a porous material is in the area of heat transfer augmentation. The Nusselt numbers for fully developed heat transfer in a channel without a porous matrix are given by expressions similar to Eqs. (4.39)–(4.42), except that the saturated porous medium conductivity k_m is replaced by the thermal conductivity of the fluid alone, k_f. The relative heat transfer augmentation effect is indicated approximately by the ratio

$$\frac{h_x(\text{with porous matrix})}{h_x(\text{without porous matrix})} \sim \frac{k_m}{k_f}, \tag{4.43}$$

in which h_x is the local heat transfer coefficient $q''/(T_w - T_b)$. In conclusion, a significant heat transfer augmentation effect can be achieved by using a high-conductivity matrix material, so that k_m is considerably greater than k_f.

Forced convection in sintered metals was investigated by Evoshenko and Yaskin (1976). An experimental study of unsteady heat transfer was reported by Koshelev et al. (1989). They obtained heat transfer coefficient much smaller than those for steady conditions. Inaba et al. (1993) reported experiments on convection in a duct of rectangular cross section, occupied by spherical particles, which was heated from below and cooled from the top. Experimental investigations were carried out by Jiang et al. (1997) for a parallel-plate channel and Kahlil et al. (2000) for a pipe. An experimental study of forced convection through microporous enhanced heat sinks was reported by Lage et al. (2004b). An experimental study of flow of CO_2 at supercritical pressure was carried out by Jiang et al. (2004i, j). Correlations for forced convection between two parallel plates or in a circular pipe were obtained by Haji-Sheikh (2004). A numerical study, using a Green's function solution method and dealing with the effects due to a temperature change at the wall and the contributions of frictional heating, was conducted by Haji-Sheikh et al. (2004a). The role of longitudinal diffusion in fully developed forced convection slug flow in a channel was studied by Nield and Lage (1998). Forced convection in a helical pipe was analyzed by Nield and Kuznetsov (2004b). Curvature of the pipe induces a secondary flow at first order and increases the Nusselt number at second order, while torsion affects the velocity at second order and does not affect the Nusslet number at second order. A numerical study of this problem was made by Cheng and Kuznetsov (2005). Gaseous slip flow in microchannels was studied by Haddad et al. (2006c, 2007b), Hooman (2009a, b), and Hashemi et al. (2011a, b). Flow in rectangular channels was treated by Haji-Sheikh (2006), Haji-Sheikh (2006), and Hooman (2008b, 2009b). Various flow orientations in a packed channel were investigated by Ma et al. (2006). Experimental work with metallic foam was

reported by Dukhan et al. (2013, 2014, 2015). A simulation and analytic validation for forced convection in metallic foams was investigated by Suleiman and Dukhan (2014). Thermally developing forced convection in a metal foam-filled elliptical annulus was studied by Benmerkhi et al. (2016). Torabi et al. (2017) performed heat transfer and entropy generation analyses using pore scale modeling.

Analytical solutions for ducts of various shapes (semi-circular, sector, super-elliptical, lens-shaped) were reported by Wang (2008, 2010a, b, 2011b).

4.6 Transient Effects

Most of the existing work on forced convection in fluid-saturated porous media is concerned with steady-state conditions. Notable exceptions are the papers on time-dependent forced convection heat transfer from an isothermal cylinder (Kimura 1989a) and from a cylinder with uniform heat flux (Kimura 1988c). Nakayama and Ebinuma (1990) studied the forced convection heat transfer between a suddenly heated plate and a non-Darcy flow that starts initially from rest.

These three papers show that the simplest and perhaps most important forced convection configuration had been overlooked. In that configuration, the flow through the saturated porous medium is steady, parallel, and uniform (Bejan and Nield 1991). The flow is driven by a pressure difference that is applied in the x-direction in Fig. 4.7, and can be either a Darcy flow or a non-Darcy flow in which the quadratic drag (Forchheimer effect) plays a role in the overall flow resistance. What distinguishes the Bejan and Nield (1991) configuration from the one analyzed by Nakayama and Ebinuma (1990) is that the flow is and remains steady as the embedded plate is suddenly heated or cooled to a different temperature.

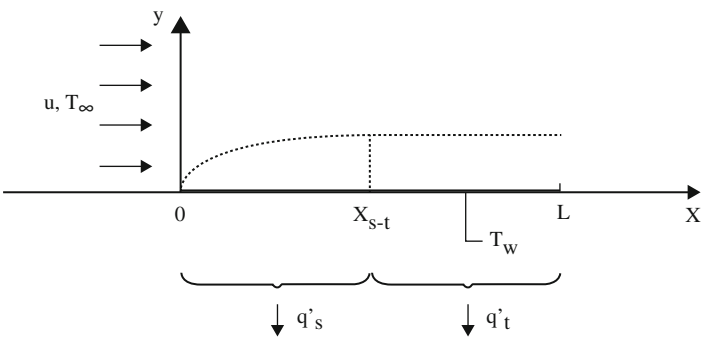

Fig. 4.7 Forced-convection thermal boundary layer near a plate embedded in a porous medium with steady, parallel, and uniform flow

4.6.1 Scale Analysis

Consider the uniform flow, with volume-averaged velocity u, which is parallel to the wall $y = 0$ shown in Fig. 4.7. The initial temperature of the fluid-saturated porous medium is T_∞. Beginning at time $t = 0$, the temperature of the wall section $0 < x < L$ is maintained at a different constant temperature, T_w. In time, the flow in the fluid-saturated porous medium adjusts to this change by developing a near-wall region wherein the variation from T_w to T_∞ is smoothed.

We can develop a feel for the size and history of the near-wall region by examining the order of magnitude implications of the energy equation for that region,

$$\sigma \frac{\partial T}{\partial t} + u \frac{\partial T}{\partial x} = \alpha_m \frac{\partial^2 T}{\partial y^2}. \tag{4.44}$$

The temperature boundary conditions are as indicated in Fig. 4.7, specifically

$$T = T_w \quad \text{at} \quad y = 0 \tag{4.45}$$

$$T \to T_\infty \quad \text{as} \quad y \to \infty \tag{4.46}$$

Implicit in the writing of the energy equation (4.42) is the assumption that the near-wall region is slender, or boundary layer-like. To this assumption we will return in Eqs. (4.62)–(4.65).

One way to perform the scale analysis is by considering the entire boundary layer region of length L. The thickness of this thermal boundary layer is denoted by δ. If we further write $\Delta T = T_\infty - T_w$, we find the following scales for the three terms of Eq. (4.42):

$$\underset{\text{thermal inertia}}{\sigma \frac{\Delta T}{t}}, \qquad \underset{\text{longitudinal convection}}{u \frac{\Delta T}{L}}, \qquad \underset{\text{transverse conduction}}{\alpha_m \frac{\Delta T}{\delta^2}}. \tag{4.47}$$

At sufficiently short times t, the transverse heating effect is balanced by the thermal inertia of the saturated porous medium. This balance yields the time-dependent thickness

$$\delta_t \sim \left(\frac{\alpha_m t}{\sigma}\right)^{1/2}. \tag{4.48}$$

As t increases, the thermal inertia scale decreases relative to the longitudinal convection scale, and the energy equation becomes ruled by a balance between transverse conduction and longitudinal convection. The steady-state boundary layer thickness scale in this second regime is

$$\delta_s \sim \left(\frac{\alpha_m L}{u}\right)^{1/2}. \tag{4.49}$$

The time of transition t_c, when the boundary layer region becomes convective, can be estimated by setting $\delta_t \sim \delta_s$:

$$t_c \sim \frac{\sigma L}{u}. \tag{4.50}$$

Not all of the L-long boundary layer is ruled by the balance between conduction and inertia when t is shorter than T_c. When t is finite, there is always a short enough leading section of length x in which the energy balance is between transverse conduction and longitudinal convection. In that section of length x and thickness δ_x, the scales of the three terms of Eq. (4.44) are

$$\sigma \frac{\Delta T}{t}, \quad u \frac{\Delta T}{x}, \quad \alpha_m \frac{\Delta T}{\delta_x^2}, \tag{4.51}$$

showing that $u\Delta T/x \sim \alpha_m \Delta T/\delta_x^2$, or

$$\delta_x \sim \left(\frac{\alpha_m x}{u}\right)^{1/2} \tag{4.52}$$

when $\sigma\ \Delta T/t < u\ \Delta T/x$, i.e., when

$$x < \frac{u t}{\sigma}. \tag{4.53}$$

The boundary layer changes from the convective (steady) section represented by Eq. (4.52) to the conductive (time-dependent) trailing section of Eq. (4.48). The change occurs at $x = x_{s-t}$ where

$$x_{s-t} \sim \frac{u t}{\sigma}. \tag{4.54}$$

4.6.2 Wall with Constant Temperature

The two-section structure of the thermal boundary layer is indicated in Fig. 4.7. Its existence was also recognized by Ebinuma and Nakayama (1990b) in the context of transient film condensation on a vertical surface in a porous medium. The chief benefit of this insight is that it enables us to delineate the regions in which two analytical solutions are known to apply, first the steady leading section where according to Eqs. (4.9)–(4.12)

$$\frac{T-T_{\mathrm{w}}}{T_{\infty}-T_{\mathrm{w}}}=\operatorname{erf}\left[\frac{y}{2}\left(\frac{u}{\alpha_{\mathrm{m}}x}\right)^{1/2}\right]\quad(x<x_{s-t}) \tag{4.55}$$

and farther downstream the time-dependent section where

$$\frac{T-T_{\mathrm{w}}}{T_{\infty}-T_{\mathrm{w}}}=\operatorname{erf}\left[\frac{y}{2}\left(\frac{\sigma}{\alpha_{\mathrm{m}}t}\right)^{1/2}\right]\quad(x>x_{s-t}). \tag{4.56}$$

The time-dependent section is no longer present when $x_{s-t}\sim L$, i.e., when $t\sim\sigma L/u$, in accordance with Eq. (4.50).

We see from the condition (4.52) that the temperature distributions (4.55) and (4.56) match at $x=x_{s-t}$. The longitudinal temperature gradient $\partial T/\partial x$ experiences a discontinuity across the $x=x_{s-t}$ cut, but this discontinuity becomes less pronounced as t increases, i.e., as the x_{s-t} cut travels downstream. It also must be said that neither Eq. (4.55) nor (4.56) is exact at $x=x_{s-t}$, because at that location none of the three effects competing in Eq. (4.45) can be neglected.

The instantaneous heat transfer rate (W/m) through the surface of length L can be deduced by taking the heat transfer rate through the leading (steady-state) section $0<x<x_{s-t}$, cf. Eq. (4.14),

$$q'_{\mathrm{s}}=k_{\mathrm{m}}\left(T_{\infty}-T_{\mathrm{w}}\right)\frac{2}{\pi^{1/2}}\left(\frac{u}{\alpha_{\mathrm{m}}}x_{s-t}\right)^{1/2} \tag{4.57}$$

and adding to it the contribution made by the time-dependent trailing section $x_{s-t}<x<L$:

$$q'_{\mathrm{t}}=(L-x_{s-t})\frac{k_{\mathrm{m}}(T_{\infty}-T_{\mathrm{w}})}{(\pi\alpha_{\mathrm{m}}t/\sigma)^{1/2}}. \tag{4.58}$$

The total heat transfer rate $q'=q'_{\mathrm{s}}+q'_{\mathrm{t}}$ can be compared with the long-time (steady-state) heat transfer rate of the L-long plate,

$$q'_{\mathrm{final}}=k(T_{\infty}-T_{\mathrm{w}})\frac{2}{\pi^{1/2}}\left(\frac{u}{\alpha_{\mathrm{m}}}L\right)^{1/2} \tag{4.59}$$

and the resulting expression is

$$\frac{q'}{q'_{\mathrm{final}}}=1+\frac{1-\tau}{2\tau^{1/2}}. \tag{4.60}$$

In this expression τ is the dimensionless time

$$\tau=\frac{ut}{\sigma L}. \tag{4.61}$$

According to Eq. (4.50), $\tau = 1$ marks the end of the time interval in which Eq. (4.60) holds. The beginning of that time interval is dictated by the validity of the assumption that the leading (steady-state) section of the boundary layer is always slender, cf. Eq. (4.49),

$$\left(\frac{\alpha_{\mathrm{m}} x_{s-t}}{u}\right)^{1/2} < x_{s-t}. \tag{4.62}$$

This requirement translates into

$$\frac{u x_{s-t}}{\alpha_{\mathrm{m}}} > 1 \tag{4.63}$$

or, in view of Eqs. (4.54) and (4.61),

$$\tau > \frac{1}{\mathrm{Pe_L}}, \tag{4.64}$$

where $\mathrm{Pe_L}$ is the Péclet number based on L,

$$\mathrm{Pe_L} = \frac{uL}{\alpha_{\mathrm{m}}}. \tag{4.65}$$

At times τ shorter than $1/\mathrm{Pe_L}$, the leading section is not a forced convection boundary layer, and the entire L length produces a time-dependent heat transfer rate of type (4.58):

$$q' = L \frac{k_{\mathrm{m}}(T_\infty - T_{\mathrm{w}})}{(\pi \alpha_{\mathrm{m}} t/\sigma)^{1/2}}. \tag{4.66}$$

The dimensionless counterpart of this estimate is

$$\frac{q'}{q'_{\mathrm{final}}} = \frac{1}{2\tau^{1/2}}. \tag{4.67}$$

In summary, the total heat transfer rate is given by three successive expressions, each for one regime in the evolution of the temperature field near the suddenly heated plate:

$$\frac{q'}{q'_{\mathrm{final}}} = \begin{cases} \dfrac{1}{2\tau^{1/2}}, & 0 < \tau < \mathrm{Pe_L^{-1}} \\ 1 + \dfrac{1-\tau}{2\tau^{1/2}}, & \mathrm{Pe_L^{-1}} < \tau < 1 \\ 1 & \tau > 1. \end{cases} \tag{4.68}$$

The domain occupied by each regime is indicated on the ($\mathrm{Pe_L}$, τ) plane of Fig. 4.8. The approximate solution (4.66) shows that relative to the long-time result (4.59), the transient heat transfer rate depends on two additional dimensionless groups, τ and $\mathrm{Pe_L}$.

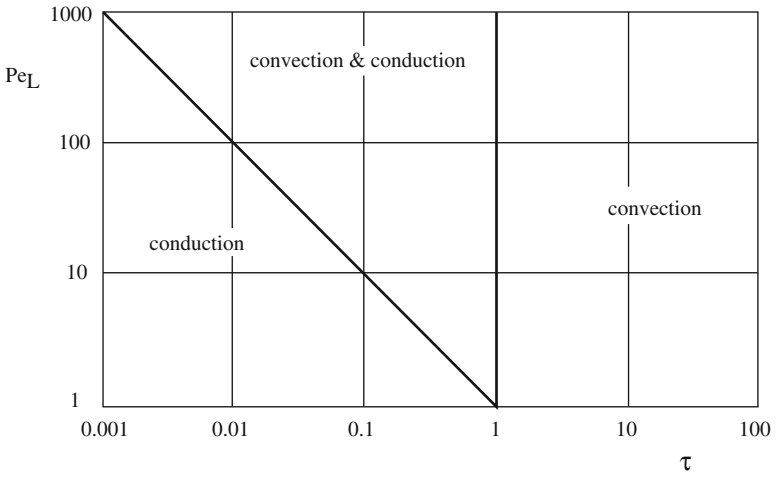

Fig. 4.8 The τ-Pe_L ranges in which the three parts of the solutions (4.66) and (4.68) are applicable

4.6.3 Wall with Constant Heat Flux

The thermal boundary layer formed in the vicinity of a plate with sudden heat flux q'' can be described in a way that is analogous to the analysis presented between Eqs. (4.55) and (4.68). The structure shown in Fig. 4.7 is present here as well, and Eqs. (4.54) and (4.61) continue to hold. The upstream portion $0 < x < x_{s-t}$ closely approximates the steady forced convection boundary layer with uniform heat flux (Sect. 4.2). The downstream section $x_{s-t} < x < L$ is dominated by time-dependent conduction into a semi-infinite medium with uniform heat flux at the surface.

The history of the L-averaged temperature of the wall or of the L-averaged wall-medium temperature difference $\overline{\Delta T}$ approaches [cf. Eq. (4.17)] the value

$$\overline{\Delta T}_{\text{final}} = \frac{4}{3\pi^{1/2}} \frac{q'' L}{k_{\text{m}}} \left(\frac{uL}{\alpha_{\text{m}}} \right)^{1/2}. \tag{4.69}$$

Expressed in dimensionless form, the L-averaged temperature difference is

$$\frac{\overline{\Delta T}}{\overline{\Delta T}_{\text{final}}} \cong \begin{cases} \dfrac{3}{2}\tau^{1/2}, & 0 < \text{Pe}_{\text{L}}^{-1} \\ \left(\dfrac{3}{3} - \dfrac{\tau}{2}\right)\tau^{1/2}, & \text{Pe}_{\text{L}}^{-1} < \tau < 1 \\ 1, & \tau > 1. \end{cases} \tag{4.70}$$

The solutions (4.66) and (4.68) are based on the assumption that $\text{Pe}_{\text{L}} \gg 1$. For example, Eq. (4.66) shows that the heat transfer ratio q'/q'_{final} experiences a change of relative magnitude $\text{O}\left(\text{Pe}_{\text{L}}^{-1}\right)$ at $\tau = \text{Pe}_{\text{L}}^{-1}$. The same observation applies to the $\Delta T/\Delta T_{\text{final}}$ ratio of Eq. (4.68).

Unsteady forced convection on a flat plate, with the effect of inertia and thermal dispersion accounted for, was analyzed by Cheng and Lin (2002). The dispersion accelerates the rate of unsteady heat transfer but does not affect the response time to reach a steady state.

4.6.4 Other Configurations

Kimura (1989b) has studied transient forced convection about a vertical cylinder. He obtained analytic solutions for small time (conduction solution) and large time (boundary layer solution) and numerical results for the general time situation. Thevenin (1995) performed other calculations.

Al-Nimr et al. (1994a, b) investigated numerically convection in the entrance region of either a tube or an annulus, when a timewise step change of wall temperature is imposed, for Darcy and non-Darcy models. A conjugate problem involving concentric annuli was studied numerically by El-Shaarawi et al. (1999). Alkam and Al-Nimr (1998) performed a numerical simulation of transient forced convection in a circular pipe partly filled with a porous substrate. Unsteady forced convection about a sphere was studied numerically by Yan and Pop (1998). Fu et al. (2001a) studied experimentally heat transfer in a channel subject to oscillating flow, while Mohamad and Karim (2001) reported experiments in a pipe with core and sheath occupied by different porous materials.

In a series of papers, Kuznetsov (1994, 1995a, b, 1996b, c, d, e, f, 1998e) investigated the effect of local thermal nonequilibrium on heat transfer, for the problem when a porous bed is initially at a uniform temperature and then suddenly subjected to a step increase of fluid inlet temperature. The locally averaged fluid velocity v is assumed to be uniform in space and constant in time. The analytical solution obtained by Kuznetsov, using a perturbation method based on the assumption that the fluid-to-solid heat transfer coefficient is large, shows that the temperature of the fluid (T_f) or solid (T_s) phase takes the form of an advancing front, while the temperature difference $T_f - T_s$ takes the form of an advancing pulse. The amplitude of that pulse decreases as the pulse propagates downstream. Kuznetsov treated in turn a one-dimensional semi-infinite region, a one-dimensional finite region, a two-dimensional rectangular region, a circular tube, a concentric tube annulus, and a three-dimensional rectangular box. In the one-dimensional semi-infinite case the wave speed v_{wave} is related to the fluid flow speed v by

$$v_{wave} = \frac{(\rho c)_f}{\varphi(\rho c)_f + (1-\varphi)(\rho c)_s} v. \tag{4.71}$$

In the two-dimensional and three-dimensional cases, the amplitude of the pulse also decreases from the central flow region to the walls of the packed bed. Kuznetsov's (1996c) paper deals with a one-dimensional slab with a fluid-to-solid heat transfer coefficient (something whose value is difficult to determine

experimentally) that varies about a mean value in a random fashion. He calculated the mean and standard deviation of $T_f - T_s$.

The effects of thermal nonequilibrium have been included in numerical simulations by Sözen and Vafai (1990, 1993), Vafai and Sözen (1990a, b), Amiri and Vafai (1994), and Amiri et al. (1995), e.g., in connection with the condensing flow of a gas or longitudinal heat dispersion in a gas flow in a porous bed. They found that the local thermal equilibrium condition was very sensitive to particle Reynolds number and Darcy number, but not to thermophysical properties. Amiri and Vafai (1998) and Wu and Hwang (1998) performed further numerical simulations.

4.7 Effects of Inertia and Thermal Dispersion: External Flow

When quadratic drag is taken into account, the Darcy equations (4.2) are replaced by the approximate equations

$$u + \frac{\chi}{\nu} u^2 = -\frac{K}{\mu} \frac{\partial P}{\partial x}, \quad v = -\frac{K}{\mu} \frac{\partial P}{\partial y} \tag{4.72}$$

for the case when the primary flow is in the x-direction, so $v/u \ll 1$. Here $\chi = c_F K^{1/2}$, where c_F was introduced in Eq. (1.12). Eliminating P from these equations and introducing the stream-function ψ defined by $u = \partial\psi/\partial y$, $v = -\partial\psi/\partial x$ so that Eq. (4.1) is satisfied, we obtain

$$\frac{\partial^2 \psi}{\partial y^2} + \frac{\chi}{\nu} \frac{\partial}{\partial y} \left[\left(\frac{\partial \psi}{\partial y} \right)^2 \right] = 0, \tag{4.73}$$

and Eq. (4.3) becomes

$$\frac{\partial \psi}{\partial y} \frac{\partial T}{\partial x} - \frac{\partial \psi}{\partial x} \frac{\partial T}{\partial y} = \alpha_m \frac{\partial^2 T}{\partial y^2}. \tag{4.74}$$

If one considers the case where $T_w = T_\infty + Ax^\lambda$, $U_\infty = Bx^m$, where A, B, λ, and m are constants, one finds that a similarity solution is possible if and only if $m = 0$ and $\lambda = 1/2$. One can check that the similarity solution is given by

$$\psi = (\alpha_m U_\infty x)^{1/2} f(\eta), \tag{4.75}$$

$$T - T_\infty = (T_w - T)\theta(\eta), \tag{4.76}$$

$$\eta = \left(\frac{U_\infty x}{\alpha_m} \right)^{1/2} \frac{y}{x}, \tag{4.77}$$

provided that f and η satisfy the differential equations

$$f''' + R^* \left[(f')^2 \right] = 0, \tag{4.78}$$

$$\theta'' = \frac{1}{2}(f'\theta - f\theta'), \tag{4.79}$$

where

$$R^* = \frac{\chi U_\infty}{\nu}. \tag{4.80}$$

The boundary conditions

$$y = 0: \quad T = T_w, \quad v = 0, \tag{4.81}$$

$$y \to \infty: \quad T = T_w, \quad u = U_\infty, \tag{4.82}$$

lead to

$$\theta(0) = 1, f(0) = 0, \ \theta(\infty) = 0, \ f'(\infty) = 1. \tag{4.83}$$

The local wall heat flux is

$$q'' = -k_m \left(\frac{\partial T}{\partial y} \right)_{y=0} = -k_m A \left(\frac{B}{\alpha_m} \right)^{1/2} \theta'(0), \tag{4.84}$$

where $\theta'(0) = -0.886$. We recognize that this is the case of constant wall heat flux. In nondimensional form this result is precisely the same as Eq. (4.16) and is independent of the value of R^*. Thus in this case quadratic drag has no effect on the wall heat flux (for fixed U_∞), but it does have the effect of flattening the dimensionless velocity profile (Lai and Kulacki 1987).

The effect of thermal dispersion in the same case was discussed by Lai and Kulacki (1989a). In the present context it is the transverse component that is important. If one allows for thermal dispersion by adding a term Cud_p (where d_p is the mean particle or pore diameter and C is a numerical constant) to α_m in the term $\alpha_m \partial^2 T/\partial y^2$ in Eq. (4.3), then Eq. (4.16) is replaced by

$$\mathrm{Nu}_x = 0.886(1 + C\,\mathrm{Pe}_d)\,\mathrm{Pe}_x^{1/2}, \tag{4.85}$$

where $\mathrm{Pe}_d = U_\infty d_p/\alpha_m$. Thus thermal dispersion increases the heat transfer because it increases the effective thermal conductivity in the y direction.

The effect of quadratic drag in the transient situation for the case of constant wall temperature was examined by Nakayama and Ebinuma (1990), who found that it

had the effect of slowing the rate at which a steady-state solution is approached. One can deduce from their steady-state formulas that (as for the constant flux situation) quadratic drag does not affect the Nu_x (Pe_x) relationship, in this book the formula (4.13).

4.8 Effects of Boundary Friction and Porosity Variation: Exterior Flow

When one introduces the Brinkman equation in order to satisfy the no-slip condition on a rigid boundary, one runs into a complex problem. The momentum equation no longer has a simple solution, and a momentum boundary layer problem must be treated. For the purposes of this discussion, we follow Lauriat and Vafai (1991) and take the boundary layer form of the momentum equation

$$\frac{1}{\varphi^2}\left(u\frac{\partial u}{\partial x}+v\frac{\partial u}{\partial y}\right)=\frac{\nu}{K}(U-u)+\frac{c_{\mathrm{F}}}{K^{1/2}}\left(U^2-u^2\right)+\frac{\nu}{\varphi}\frac{\partial^2 u}{\partial y^2}. \tag{4.86}$$

For the reasons pointed out in Sect. 1.5, we drop the left-hand side of this equation at the outset, and in the last term we replace φ^{-1} by $\widetilde{\mu}/\mu$. The condition on a plane wall is now

$$u=v=0,\quad T=T_{\mathrm{w}}\quad \text{for } x>0, y=0. \tag{4.87}$$

The remaining equations and boundary conditions are unaltered.

The integral method, as used by Kaviany (1987), provides an approximate solution of the system. If the velocity profile is approximated by

$$u=U_\infty\left[\frac{3}{2}\frac{y}{\delta}-\frac{1}{2}\left(\frac{y}{\delta}\right)^3\right], \tag{4.88}$$

one finds that the momentum boundary layer thickness δ is given by

$$\frac{\delta^2}{K/\varphi}=\frac{140}{\left(35+48c_{\mathrm{F}}\mathrm{Re}_{\mathrm{p}}\right)}\left(1-\mathrm{e}^{-\gamma x^*}\right) \tag{4.89}$$

where

$$\mathrm{Re}_{\mathrm{p}}=U_\infty K^{1/2}/\nu \tag{4.90}$$

is the pore Reynolds number

$$\gamma=\left(\frac{70}{13}\frac{1}{\mathrm{Re}_{\mathrm{p}}}+\frac{96}{13}c_{\mathrm{F}}\right)\varphi^{3/2}, \tag{4.91}$$

and

$$x^* = \frac{x}{(K/\varphi)^{1/2}}. \tag{4.92}$$

The momentum boundary layer thickness δ is almost constant when $x^* > 5/\gamma$. Thus the hydrodynamic development length can be taken as

$$x_e = \frac{5}{\gamma}\left(\frac{K}{\varphi}\right)^{1/2} \tag{4.93}$$

and the developed momentum boundary layer thickness is given by

$$\delta = \left[\left(\frac{140}{35 + 48\, c_F \mathrm{Re}_p}\right)\frac{K}{\varphi}\right]^{1/2}. \tag{4.94}$$

For the developed region, exact solutions have been obtained by Cheng (1987), Beckermann and Viskanta (1987), and Vafai and Thiyagaraja (1987). They show that the velocity is constant outside a boundary layer whose thickness decreases as c_F and/or Re_p increases, in accordance with Eq. (4.86).

Wall effects caused by nonuniform porosity (Sect. 1.7) have been investigated experimentally by a number of investigators and theoretically by Vafai (1984, 1986), Vafai et al. (1985), and Cheng (1987). The degree to which hydrodynamic wall effects influence the heat transfer from a heated wall depends on the Prandtl number Pr of the fluid. The ratio of the thermal boundary layer thickness δ_T to the momentum boundary layer thickness δ is of order Pr^{-1}. For low Prandtl number fluids ($\mathrm{Pr} \to 0$), $\delta \ll \delta_T$ and the temperature distribution, and hence the heat transfer, is given by the Darcy theory of Sects. 4.1 and 4.2. For a more general case where the inertial effects are taken into account and for a variable wall temperature in the form $T_w = T_\infty + Ax^p$, an exact solution was obtained by Vafai and Thiyagaraja (1987) for low Prandtl number fluids in terms of gamma and parabolic cylindrical functions. They found the temperature distribution to be

$$T = T_\infty + A\Gamma(p+1) \times \left\{2^{p+1/2}\,\pi^{-1/2}\,x^p \exp\left(-\alpha y^2/x\right) D_{-(2p+1)}\left[\left(4\alpha y^2/x\right)^{1/2}\right]\right\}, \tag{4.95}$$

where $\alpha = U_\infty/8\alpha_m$. The corresponding local Nusselt number is

$$\mathrm{Nu}_x = \frac{\Gamma(p+1)}{\Gamma(p+1/2)}\left(\mathrm{Re}_p\,\mathrm{Pr}_e\right)^{1/2}, \quad \mathrm{Da}_x^{-1/4} = \frac{\Gamma(p+1)}{\Gamma(p+1/2)}\mathrm{Pe}_x^{1/2}, \tag{4.96}$$

which reduces to Eq. (4.13) when $p = 0$.

When the Prandtl number is very large, $\delta_T \ll \delta$ and so the thermal boundary layer lies completely inside the momentum boundary layer. As $\mathrm{Pr} \to \infty$ one can assume that the velocity distribution within the thermal boundary layer is linear and given by

$$u = \frac{\tau_w y}{\mu_f}, \tag{4.97}$$

where τ_w is the wall stress which is given by

$$\tau_w = \frac{\mu_f U_\infty}{(K/\varphi)^{1/2}} \left(1 + \frac{4}{3} c_F \mathrm{Re}_p\right)^{1/2}. \tag{4.98}$$

This means that the energy equation can be approximated by

$$y \frac{\partial T}{\partial x} = \frac{\alpha_m \mu_f}{\tau_w} \frac{\partial^2 T}{\partial y^2}. \tag{4.99}$$

We now introduce the similarity variables

$$\eta = y \left(\frac{1}{9\xi x}\right)^{1/3}, \quad \theta(\eta) = \frac{T - T_w}{T_\infty - T_w}, \tag{4.100}$$

where

$$\xi = \frac{\alpha_m \mu_f}{\tau_w} = \frac{K}{\mathrm{Re}_p \mathrm{Pr}_e} \left[\varphi \left(1 + \frac{4}{3} c_F \mathrm{Re}_p\right)\right]^{-1/2} \tag{4.101}$$

and where the *effective* Prandtl number Pr_e is defined as

$$\mathrm{Pr}_e = \frac{\nu}{\alpha_m}. \tag{4.102}$$

We then have the differential equation system

$$\theta'' + 3\eta^2 \theta' = 0, \tag{4.103}$$

$$\theta(0) = 0, \quad \theta(\infty) = 1, \tag{4.104}$$

which has the solution (Beckermann and Viskanta 1987)

$$\theta = \frac{1}{\Gamma(4/3)} \int_0^\eta e^{-\xi^3} d\xi. \tag{4.105}$$

Hence the local Nusselt number is

$$\begin{aligned} \mathrm{Nu_x} &= \frac{k_\mathrm{m}\,(\partial T/\partial y)_{y=0}}{k_\mathrm{m}\,(T_\mathrm{w}-T_\infty)/x} = 1.12\left(\frac{x^2}{9\xi}\right)^{1/3} \\ &= 0.538\left[\varphi\left(1+\tfrac{4}{3}c_\mathrm{F}\mathrm{Re_p}\right)\right]^{1/6}\left(\frac{\mathrm{Re_p\,Pr_e}}{\mathrm{Da_x}}\right)^{1/3} \end{aligned} \tag{4.106}$$

and the overall Nusselt number over a length L from the leading edge becomes

$$\overline{\mathrm{Nu}} = 1.68\left(\frac{L^2}{9\xi}\right)^{1/3}. \tag{4.107}$$

Vafai and Thiyagaraja (1987) compared these analytical results with numerical solutions. They found that the low Prandtl number analytical solution accurately predicts the temperature distribution for a Prandtl number $\mathrm{Pr_e}$ as high as 8, while the high-$\mathrm{Pr_e}$ analytical solution is valid for $\mathrm{Pr_e}$ as low as 100 and possibly for somewhat lower values.

The combined effects of inertia and boundary friction were considered by Kaviany (1987). He expressed his results in terms of a parameter Γ_x defined as the total flow resistance per unit volume (Darcy plus Forchheimer drag) due to the solid matrix, scaled in terms of $8\rho U_\infty^2/3\varphi x$. He concluded that the "Darcian regime" where $\mathrm{Nu_x}$ varies as $\mathrm{Pr_e^{1/2}}$ holds when $\Gamma_\mathrm{x} > 0.6\ \mathrm{Pr_e}$ and the "non-Darcian regime" where $\mathrm{Nu_x}$ varies as $\mathrm{Pr_e^{1/3}}$ holds when $0.07 < \Gamma_\mathrm{x} < 0.6\ \mathrm{Pr_e}$. When $\Gamma_\mathrm{x} = 0.07$ the presence of the solid matrix is not significant. Another study is that by Kumari et al. (1990c).

Vafai et al. (1985) experimentally and numerically investigated the effects of boundary friction and variable porosity. Their experimental bed consisted of glass beads of 5 mm and 8 mm diameter saturated with water. They found good agreement between observation of the average Nusselt number and numerical predictions when the effect of variable porosity was included (but not otherwise). Cheng (1987) noted that since their experiments were conducted in the range $100 < \mathrm{Re_p} < 900$, thermal dispersion effects should have been important, and in fact they neglected these. He pointed out that in their numerical work Vafai et al. (1985) used a value of thermal conductivity about three times larger than was warranted, and by doing so they had fortuitously approximated the effect of transverse thermal dispersion.

Further experimental work was undertaken by Renken and Poulikakos (1989a). They reported details of thermal boundary layer thickness, temperature field, and local Nusselt number. Good agreement was found with the numerical results of Vafai et al. (1985) with the effects of flow inertia and porosity variation accounted for. Further work was done by Hayes (1990a).

Some further details on the content of this section can be found in the review by Lauriat and Vafai (1991). Nakayama et al. (1990a) used novel transformed

variables to produce a local similarity solution for flow over a plate. Vafai and Kim (1990) analyzed flow in a composite medium consisting of a fluid layer overlaying a porous substrate that is attached to the surface of a plate. Luna and Mendez (2005a, b) used a Brinkman model to study analytically and numerically the conjugate problem of forced convection on a plate with finite thermal conductivity and with constant heat flux at the extreme boundary.

For the case of cross flow across a cylinder, Fand et al. (1993) obtained empirical correlation expressions for the Nusselt number. For the same geometry, a numerical study was made by Nasr et al. (1995). They reported that the effect of decreasing Da was an increase in Nu, but Lage and Nield (1997) pointed out that this is true only if the Reynolds number Re is held constant. If the pressure gradient is kept constant, Nu increases with Da. Nasr et al. (1995) also noted that Nu increased with an increase of either Re or effective Prandtl number, and that the effect of quadratic drag on Nu is via the product DaRe.

Heat transfer around a periodically heated cylinder was studied experimentally (with water and glass beads) and numerically by Fujii et al. (1994). They also modeled the effects of thermal dispersion and thermal nonequilibrium. Conjugate flow around a cylinder with internal heat generation was studied by Kadir et al. (2008).

Unsteady forced convection, produced by small amplitude variations in the wall temperature and free stream velocity, along a flat plate was studied by Hossain et al. (1996).

The effect of viscous dissipation was discussed by Aydin and Koya (2008b, c, d), Rees and Magyari (2008), and Nield (2008a). The effect of variable viscosity and variable Prandtl number was studied by Pantokratoras (2007c).

4.9 Effects of Boundary Friction, Inertia, Porosity Variation, Thermal Dispersion, and Axial Conduction: Confined Flow

In porous channels the velocity field generally develops to its steady-state form in a short distance from the entrance. To see this, let t_c be a characteristic time for development and u_c a characteristic velocity. During development the acceleration term is of the same order of magnitude as the Darcy resistance term, so $u_c/t_c \sim \nu\, u_c/K$, and so the development length $\sim t_c u_c \sim K u_c/\nu$, which is normally small. [Note that, in contrast with the argument used by Vafai and Tien (1981), the present argument holds whether or not the convective inertial term is negligible.] Further, the numerical results of Kaviany (1985) for flow between two parallel plates show that the entrance length decreases linearly as the Darcy number decreases. In this section we assume that the flow is also fully developed thermally.

We start by considering a channel between two plane parallel walls a distance $2H$ apart, the boundaries being at $y = H$ and $y = -H$. For fully developed flow the velocity is $u(y)$ in the x-direction. We suppose that the governing equations are

$$G = \frac{\mu u^*}{K} + \frac{c_{\mathrm{F}} \rho u^{*2}}{K^{1/2}} - \widetilde{\mu} \frac{d^2 u^*}{dy^{*2}}, \tag{4.108}$$

$$u^* \frac{\partial T^*}{\partial x^*} = \frac{k_{\mathrm{m}}}{(\rho c_{\mathrm{P}})_{\mathrm{f}}} \frac{\partial^2 T^*}{\partial y^{*2}}. \tag{4.109}$$

Here the asterisks denote dimensional variables, and G is the applied pressure gradient. Local thermal equilibrium has been assumed, dispersion is neglected, and it is assumed that the Péclet number is sufficiently large for the axial thermal conduction to be insignificant. We define the dimensionless variables

$$x = \frac{x^*}{H}, \quad y = \frac{y^*}{H}, \quad u = \frac{\widetilde{\mu} u^*}{GH^2}, \tag{4.110}$$

and write

$$M = \frac{\widetilde{\mu}}{\mu}, \quad \mathrm{Da} = \frac{K}{H^2}, \quad F = \frac{c_{\mathrm{F}} \rho G H^4}{K^{1/2} \mu^2}. \tag{4.111}$$

Thus M is a viscosity ratio, Da is a Darcy number, and F is a Forchheimer number. Then Eq. (4.108) becomes

$$M \frac{d^2 u}{dy^2} - \frac{u}{\mathrm{Da}} - F u^2 + 1 = 0. \tag{4.112}$$

This equation is to be solved subject to the boundary/symmetry conditions

$$u = 0 \quad \text{at} \quad y = 1, \qquad \frac{du}{dy} = 0 \quad \text{at} \quad y = 0. \tag{4.113}$$

When F is not zero, the solution can be expressed in terms of standard elliptic functions (Nield et al. 1996). When $F = 0$, the solution is

$$u = \mathrm{Da}\left(1 - \frac{\cosh Sy}{\cosh S}\right), \tag{4.114}$$

where for convenience we introduce

$$S = \frac{1}{(M\mathrm{Da})^{1/2}}. \tag{4.115}$$

We also introduce the mean velocity U^* and the bulk mean temperature T^*_{m} defined by

$$U^* = \frac{1}{H}\int_0^H u^* dy^*, \quad T_{\mathrm{m}}{}^* = \frac{1}{HU^*}\int_0^H u^* T^* dy^*. \tag{4.116}$$

We then introduce further dimensionless variables defined by

$$\widehat{u} = \frac{u^*}{U^*}, \quad \widehat{T} = \frac{T^* - T^*_w}{T^*_{\mathrm{m}} - T^*_{\mathrm{w}}}, \tag{4.117}$$

and the Nusselt number

$$\mathrm{Nu} = \frac{2Hq''}{k_{\mathrm{m}}\left(T^*_{\mathrm{m}} - T^*_{\mathrm{w}}\right)}. \tag{4.118}$$

Here T^*_{w} and q'' are the temperature and heat flux on the wall.

For the case of uniform heat flux on the boundary, the first law of thermodynamics leads to

$$\frac{\partial T^*}{\partial x^*} = \frac{dT^*_{\mathrm{m}}}{dx^*} = \frac{q''}{(\rho c_{\mathrm{P}})_{\mathrm{f}} HU^*} = \text{constant}. \tag{4.119}$$

In this case Eq. (4.109) becomes

$$\frac{d^2\widehat{T}}{dy^2} = -\frac{1}{2}\mathrm{Nu}\,\widehat{u}. \tag{4.120}$$

The boundary conditions for this equation are

$$\widehat{T} = 0 \quad \text{at } y = 1, \qquad \frac{d\widehat{T}}{dy} = 0 \quad \text{at} \quad y = 0. \tag{4.121}$$

For the Brinkman model, with u given by Eq. (4.114), we have

$$\widehat{u} = \frac{S}{S - \tanh S}\left(1 - \frac{\cosh Sy}{\cosh S}\right), \tag{4.122}$$

$$\widehat{T} = \frac{S\,Nu}{S - \tanh \mathrm{S}}\left[\frac{1}{4}\left(1 - y^2\right) - \frac{\cosh S - \cosh Sy}{2S^2 \cosh S}\right]. \tag{4.123}$$

The definition of the dimensionless temperature leads to an identity that we call the integral compatibility condition (Nield and Kuznetsov 2000), namely

$$\int_0^1 \widehat{u}\widehat{T}\,dy = 1. \tag{4.124}$$

Substitution from Eqs. (4.122) and (4.123) then leads to

$$\mathrm{Nu} = \frac{12S(S - \tanh S)^2}{2S^3 - 15S + 15\tanh S + 3S\tanh^2 S}, \tag{4.125}$$

in agreement with an expression obtained by Lauriat and Vafai (1991). As the Darcy number Da increases from 0 to ∞, i.e., as S decreases from ∞ to 0, the Nusselt number Nu decreases from the Darcy value 6 [agreeing with Eq. (4.42)] to the clear fluid value 210/51 = 4.12. Thus the effect of boundary friction is to decrease the heat transfer by reducing the temperature gradient at the boundary.

For $F \neq 0$, Vafai and Kim (1989) used a boundary-layer approximation in obtaining a closed-form solution. This solution becomes inaccurate for hyperporous media, those for which Da > 0.1. For such media, the Brinkman term is comparable with the Darcy term throughout the flow (and not just near the walls) and K can no longer be determined by a simple Darcy-type experiment. A closed-form solution of the Brinkman–Forchheimer equation, valid for all values of Da, was obtained by Nield et al. (1996). Some typical results are given in Fig. 4.9.

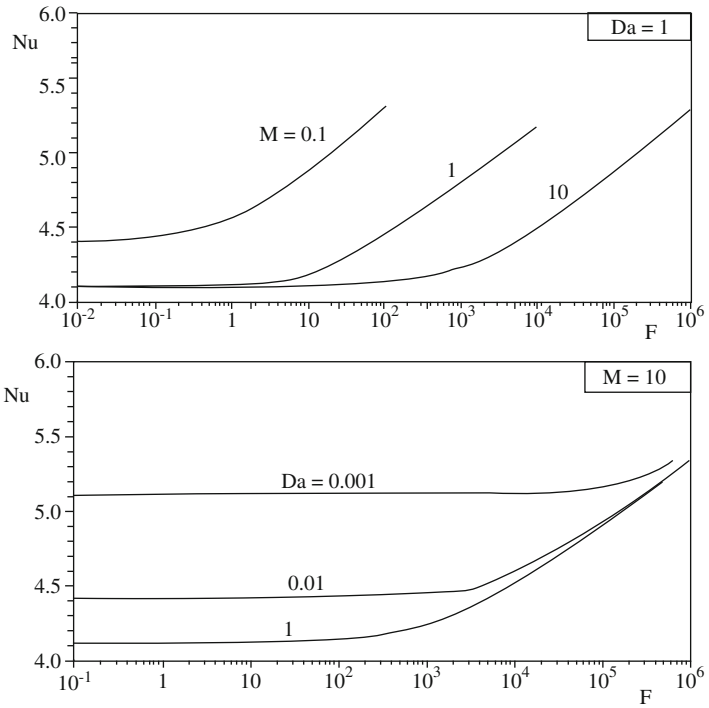

Fig. 4.9 Effect of the Forchheimer number, F, on the Nusselt number Nu, for a channel with isoflux boundaries (Nield et al. 1996)

The results of Nield et al. (1996) may be summarized as follows. For each type of thermal boundary condition, the temperature profile is little changed as a result of variation of M, Da, or F. It is slightly more peaked when Da is small or when F is large. On the other hand, the Nusselt number is significantly altered, primarily as a result of the change in velocity profile. The effect of an increase in F is to produce a more slug-like flow; and because of the way the mean velocity is defined this decreases $(T_w - T_m)$, and hence increases Nu. In particular, for the case of isoflux boundaries, the following holds. When simultaneously Da is large and F is small, the velocity profile is approximately parabolic and the Nusselt number is near 70/17 (a lower bound). When either Da is sufficiently small or F is sufficiently large, the velocity profile is approximately uniform (apart from a thin boundary layer) and the Nusselt number is near 6 (an upper bound). For the case of isothermal surfaces the story is similar, but the Nusselt numbers are smaller [the reason for this is spelled out in Nield et al. (1996, p. 211)].

An exact analytical solution was also presented by Abbasbandy et al. (2011).

For the case of a circular tube, with H replaced by the radius R of the tube in the scaling, one finds (Nield et al. 2003b) that the solution can be expressed in terms of modified Bessel functions:

$$\widehat{u} = \frac{S[I_0(S) - I_0(Sr)]}{SI_0(S) - 2I_1(S)}, \tag{4.126}$$

$$\widehat{T} = \frac{S\,\mathrm{Nu}}{SI_0(S) - 2I_1(s)}\left[\frac{I_0(S)}{4}\left(1 - r^2\right) - \frac{I_0(S) - I_0(Sr)}{S^2}\right], \tag{4.127}$$

$$\mathrm{Nu} = \frac{8S[SI_0(S) - 2I_1(S)]^2}{\left(S^3 - 24S\right)[I_0(S)]^2 + 48I_0(S)I_1(S) + 8S[I_1(S)]^2}. \tag{4.128}$$

When the uniform flux boundary condition is replaced by the uniform temperature condition, one finds that Eq. (4.120) is replaced by

$$\frac{d^2\widehat{T}}{dy^2} = -\frac{1}{2}\mathrm{Nu}\,\widehat{u}\widehat{T}. \tag{4.129}$$

The boundary condition given by Eq. (4.121) still applies. We see that we now have an eigenvalue problem with Nu as the eigenvalue. Now Eq. (4.124) is satisfied trivially, and instead of this compatibility condition one uses a differential compatibility condition (previously satisfied trivially), namely

$$\mathrm{Nu} = -2\frac{d\widehat{T}}{dy}(1). \tag{4.130}$$

Equation (4.130) enables the amplitude of the eigenfunction to be determined. For the case of Darcy flow (Da = 0) we have $\widehat{u} = 1$, $\widehat{T} = (\pi/2)\cos(\pi y/2)$ and $\mathrm{Nu} = \pi^2/2 = 4.93$. For other values of Da the value of Nu can be found numerically,

most readily by expressing the second-order differential equation as two first-order equations and then using a shooting method. Details of the method may be found in Nield and Kuznetsov (2000).

The above results for symmetric heating can be extended to the case of asymmetric heating, using a result established by Nield (2004c). The result applies when the heat flux along each boundary is uniform, or the temperature along each boundary is uniform. With the Nusselt number defined in terms of the mean wall temperature and the mean wall heat flux, the value of the Nusselt number is independent of the asymmetry whenever the velocity profile is symmetric with respect to the midline of the channel. This means that the above results also apply to the case of heating asymmetric with respect to the midline. Further work involving asymmetric heat flux boundary conditions was reported by Mitrovic and Maletic (2006, 2007) and Cezmer et al. (2011). Experiments with asymmetrically heated channels filled with glass beads were performed by Jeng et al. (2011). Mondal (2013) reported an analytical study of thermodynamically consistent limiting forced convection in an asymmetrically heated channel.

In the case of a circular tube, Eqs. (4.129) and (4.130) are replaced by

$$\frac{d^2\widehat{T}}{dr^2}+\frac{1}{r}\frac{d\widehat{T}}{dr}=-\mathrm{Nu}\,\widehat{u}\widehat{T}, \tag{4.131}$$

$$\mathrm{Nu}=-2\frac{d\widehat{T}}{dr}(1). \tag{4.132}$$

For the case $\mathrm{Da}=0$ one finds that $\mathrm{Nu}=\lambda^2$ where $\lambda=2.40483$ is the smallest positive root of the Bessel function $J_0(x)$, so that $\mathrm{Nu}=(2.40483)^2=5.783$, and $\widehat{T}=\lambda J_0(\lambda r)/2J_1(\lambda)$.

Variable porosity effects in a channel bounded by two isothermal parallel plates and in a circular pipe were examined numerically by Poulikakos and Renken (1987), for the case of a fully developed velocity field. They assumed that the porosity variation had negligible effects on the thermal conductivity, an assumption that breaks down when there is a large difference between the thermal conductivities of the two phases (David et al. 1991). Poulikakos and Renken (1987) found that in the fully developed region the effect of channeling was to produce a Nusselt number increase (above the value based on the Darcy model) of 12% for a parallel-plate channel and 22% for a circular pipe.

Renken and Poulikakos (1988) performed an experimental investigation for the parallel-plate configuration with the walls maintained at constant temperature, with particular emphasis on the thermally developing region. They also performed numerical simulations incorporating the effects of inertia, boundary friction, and variable porosity. Their experimental and numerical findings agreed on predicting an enhanced heat transfer over that predicted using the Darcy model.

Poulikakos and Kazmierczak (1987) obtained closed-form analytical solutions of the Brinkman equation for parallel plates and a circular pipe with constant heat flux on the walls for the case where there is a layer of porous medium adjacent to the

walls and clear fluid interior. They also obtained numerical results when the walls were at constant temperature. For all values of Da the Nusselt number Nu goes through a minimum as the relative thickness of the porous region s varies from 0 to 1. The minimum deepens and is attained at a smaller value of s as Da increases. A general discussion of Brinkman, Forchheimer, and dispersion effects was presented by Tien and Hunt (1987). For the Brinkman model and uniform heat flux boundaries, Nakayama et al. (1988a, b) obtained exact and approximate solutions. Analytical studies giving results for small or large Darcy numbers for convection in a circular tube were reported by Hooman and Ranjbar-Kani (2003, 2004). An analytical solution for the case of the Poiseuille-Couette combination for entry profiles was reported by Ansari and Siddiqui (2010).

Hunt and Tien (1988a) have performed experiments that document explicitly the effects of thermal dispersion in fibrous media. They were able to correlate their Nusselt number data, for high Reynolds number flows, in terms of a parameter $u_a L^{1/2} K^{1/4}/\alpha_m$, where u_a is the average streamwise Darcy velocity and L is a characteristic length. Since this parameter does not depend explicitly on the thermal conductivity, they concluded that dispersion overwhelmed transport from solid conduction. They were able to explain this behavior using a dispersion conductivity of the form

$$k_d = \rho c_P \gamma K^{1/2} u, \tag{4.133}$$

where γ is a numerical dispersion coefficient, having the empirically determined value of 0.025. An analytical study of the effect of transverse thermal dispersion was reported by Kuznetsov (2000c). A theoretical analysis with the Brinkman model of the case of a parallel-plate channel with uniform heat flux was made by Hooman and Dahari (2015).

Hunt and Tien (1988b) modeled heat transfer in cylindrical packed beds such as chemical reactors by employing a Forchheimer–Brinkman equation. They allowed the diffusivity to vary across the bed. Marpu (1993) found that the inclusion of axial conduction leads to a significant increase in Nusselt number in the thermally developing region of pipes for Péclet number less than 100. In similar circumstances, the effect of axial dispersion was found by Adnani et al. (1995) to be important for Péclet number less than 10.

Cheng et al. (1991) reviewed methods for the determination of effective radial thermal conductivity and Nusselt number for convection in packed tubes and channels and reanalyzed some of the previous experimental data in the light of their own contributions to thermal dispersion theory with variable porosity effects taken into account. They found that for forced convection in a packed column the average Nusselt number depends not only on the Reynolds number but also on the dimensionless particle diameter, the dimensionless length of the tube, the thermal conductivity ratio of the fluid phase to the solid phase, and the Prandtl number of the fluid. They summarized their conclusions by noting that in their work [Cheng et al. 1988; Cheng and Hsu 1986a, b; Cheng and Zhu 1987; Cheng and Vortmeyer 1988;

Hsu and Cheng 1988, 1990] they had developed a consistent theory for the study of forced convection in a packed column taking into consideration the wall effects on porosity, permeability, stagnant thermal conductivity, and thermal dispersion. These effects become important as the particle/tube diameter ratio is increased. Various empirical parameters in the theory can be estimated by comparison of theoretical and experimental results for the pressure drop and heat transfer, but there is at present a need to perform more experiments on forced convection in packed columns where both temperature distribution and heat flux are measured to enable a more accurate determination of the transverse thermal dispersivity.

Chou et al. (1994) performed new experiments and simulations for convection in cylindrical beds. They concluded that discrepancies in some previous models could be accounted for by the effect of channeling for the case of low Péclet number and the effect of thermal dispersion in the case of high Péclet number. Chou et al. (1992b, c) had reported similar conclusions, on the basis of experiments, for convection in a square channel.

The effect of suction at permeable walls was investigated by Lan and Khodadadi (1993). An experimental study of convection with asymmetric heating was reported by Hwang et al. (1992). Bartlett and Viskanta (1996) obtained analytical solutions and did experiments for thermally developing convection in an asymmetrically heated duct filled with a medium of high thermal conductivity.

Lage et al. (1996) performed a numerical study for a device (designed to provide uniform operating temperatures) consisting of a microporous layer placed between two sections of a cold plate. The simulation was based on two-dimensional equations derived from three-dimensional equations by integration over the small dimension of the layer.

For convection in cylindrical beds, Kamiuto and Saitoh (1994) investigated Nu_P, κ, and Γ, where Nu_P and Re_P are Nusselt and Reynolds numbers based on the particle diameter, while κ is the ratio of thermal conductivity of solid to that of fluid and Γ is the ratio of bed radius to particle diameter. They found that as Re_PPr tends to zero, Nu_P tends to a constant value depending on both κ and Γ, while for large Re_PPr the value of Nu_P depends on both Re_PPr and Pr but only to a small extend on κ.

For pipes packed with spheres, Varahasamy and Fand (1996) have presented empirical correlation equations representing a body of new experimental data. Experimental studies involving metal foams have been reported by Calmidi and Mahajan (2000), Hwang et al. (2002), and Zhao et al. (2004b). Further experimental and theoretical studies of convection in a circular pipe were conducted by Izadpanah et al. (1998). Extending previous experimental work by Jiang et al. (1999b), Li et al. (2003), Xu and Jiang (2004), Jiang et al. (2004e, f, h), Jiang and Liu (2006) studied numerically and experimentally the wall porosity effect for a sintered porous medium. A similar study of non-sintered material was reported by Jiang et al. (2004g). Sintered materials also were discussed by Kim and Kim (2000). Forced convection in microstructures was discussed by Kim and Kim (1999). Another numerical study in a metallic fibrous material was reported by Angirasa (2002a), and that was followed with an experimental study by Angirasa (2002b). An experimental study with aluminum foam in an asymmetrically heated channel

was made by Kim et al. (2001b). Experimental studies of structured packed beds were made by Yang et al. (2012a, b, c).

Entropy generation in a rectangular duct was studied by Demirel and Kahraman (1999). For a square duct, a numerical study of three-dimensional flow was reported by Chen and Hadim (1999b). Unsteady convection in a square cylinder was studied numerically by Perng et al. (2011).

The effect of viscous dissipation has been studied numerically by Zhang et al. (1999c) for a parallel-plate channel and by Yih and Kamioto for a circular pipe. An analytical study of the effects of both viscous dissipation and flow work in a channel, for boundary conditions of uniform temperature or uniform heat flux, was reported by Nield et al. (2004b). These authors specifically satisfied the first law of thermodynamics when treating the fully developed flow. They also considered various models for the contribution from the Brinkman term to the viscous dissipation. Further work involving viscous dissipation was reported by Costa et al. (2004c), Hooman and Gorji-Bandpy (2004), Hung and Tso (2008, 2009) and (with nonlinear drag) Rassoulineajad-Mousavi and Yaghoobi (2014).

The effect of axial conduction in channels and tubes was studied by Minkowycz and Haji-Sheikh (2006, 2009) and Haji-Sheikh et al. (2010a, b). The effect of Forchheimer quadratic drag in rectangular ducts was examined by Akyidiz and Siginer (2011).

For a circular tube and the Brinkman–Forchheimer model, asymptotic solutions for small and large Darcy numbers were reported by Hooman and Gurgenci (2007a, b, c) while Rassoulinejad-Mousavi and Abbasbandy (2011) obtained results using spectral homotopy analysis. Barletta et al. (2016) studied unstable forced convection in a plane porous channel with variable-viscosity dissipation. Zallama et al. (2016a, b) investigated viscous dissipation generation in an adiabatic cylinder and a channel.

Some general matters related to the possibility of fully developed convection were discussed by Nield (2006). An analytical study of heat transfer in Couette flow was made by Kuznetsov (1998c). An analytical treatment of Couette-Poiseuille flow was reported by Aydin and Avci (2011). An analytical study of a conjugate problem, with conduction heat transfer inside the channel walls accounted for, was made by Mahmud and Fraser (2004a, b). Entropy generation in a channel was studied analytically and numerically by Mahmud and Fraser (2005b). Vafai and Amiri (1998) briefly surveyed some of the work done on the topics that here are discussed mainly in Sects. 4.9 and 4.10.

Convection in a hyperporous medium saturated by a rarefied gas, with both velocity slip and temperature slip at the boundaries of a parallel-plate channel or a circular duct, was analyzed by Nield and Kuznetsov (2006a, 2007a) and discussed by Al-Nimr and Haddad (2006) and Hashemi and Fazeli (2010). They found that temperature slip leads to decreased transfer, while the effect of velocity slip depends on the geometry and the Darcy number. Shokouhmand et al. (2010) reported results for flow in micro- and nanochannels for a wide range of Knudsen number. Further work on slip flow in microchannels has been done by Chauhan and Kumar (2009), Hooman et al. (2009b), Meghdadi et al. (2012), Vu et al. (2014), and Dehghan et al. (2015a).

4.10 Local Thermal Nonequilibrium

It is now commonplace to employ a two-temperature model to treat forced convection with local thermal nonequilibrium (LTNE). Authors who have done this include Vafai and Tien (1989), Jiang et al. (1998, 1999a, b, 2000, 2002), Jiang and Ren (2001), You and Song (1999), Kim et al. (2000a, 2000b), Kim and Jang (2002), Muralidhar and Suzuki (2001), Kuwahara et al. (2000), Nakayama et al. (2001), Foo et al. (2005), Moghari (2008), and Hayes et al. (2008). Haddad et al. (2006a, 2007a) studied gas flow in microchannels; Chen and Tsao (2011b) studied the effect of viscous dissipation. Microchannels were also investigated by Buonomo et al. (2014b). Conjugated heat transfer in a double-pipe filled with metallic foam was studied numerically by Du et al. (2010). A MHD boundary layer past a porous substrate was treated by Jat and Chaudhary (2009).

Transient and time-periodic convection in a channel has been treated analytically by Al-Nimr and Abu-Hijleh (2002), Al-Nimr and Kiwan (2002), Abu-Hijleh et al. (2004), Khashan et al. (2005), and Forooghi et al. (2011). A further study of transient convection was conducted by Spiga and Morini (1999). An analysis involving a perturbation solution was presented by Kuznetsov (1997d). The specific aspect of LTNE involving steady convective processes was analyzed by Nield (1998a). The modeling of local nonequilibrium in a structured medium was discussed by Nield (2002), and a conjugate problem was analyzed by Nield and Kuznetsov (1999). A problem in a channel with one wall heated was analyzed by Zhang and Huang (2001); see also the note by Magyari and Keller (2002). The departure from local thermal equilibrium due to a rapidly changing heat source was analyzed by Minkowycz et al. (1999). Further analysis was carried out by Lee and Vafai (1999) and Marafie and Vafai (2001). The particular case of various models for constant wall heat flux boundary conditions was discussed by Alazmi and Vafai (2002). The present authors think that the best model is the one where there is uniform flux over the two phases, as employed by Nield and Kuznetsov (1999). Alazmi and Vafai (2004) showed that thermal dispersion has the effect of increasing the sensitivity of LTNE between the two phases. The case of a non-Newtonian fluid was treated numerically by Khashan and Al-Nimr (2005). Most work on LTNE has been done for confined flows, but Wong et al. (2004) treated finite Péclet number effects in forced convection past a heated cylinder and Kwan et al. (2008) studied convection past a sphere at finite Péclet number.

The effect of LTNE on minimal resistance of layered systems was treated by Leblond and Gosselin (2008). A general criterion for local thermal equilibrium was proposed by Zhang and Liu (2008) and Zhang et al. (2009a, b, c).

Celli et al. (2010) studied a steady 2D boundary layer flow. They noted that when the basic flow is high the two thermal fields are described accurately using the boundary layer approximation. They analyzed the resulting parabolic system analytically and numerically, and found that the LTNE effects are strongest near the leading edge and equilibrium is attained at large distances.

Fully developed forced convection in a tube was further analyzed by Yang et al. (2011a). Imani et al. (2012) numerically simulated convection through an array of disconnected conducting cylindrical fins.

Yang and Vafai (2010, 2011a, b, c) have produced analytical solutions for convection with LTNE based on various alternative boundary conditions. Klinbun et al. (2012) included the effect of LTNE in their study and the effect of a transient electromagnetic field on forced convection in a waveguide filled with porous material. Convection from a circular cylinder was studied by Al-Sumaily et al. (2013). Dukhan and Al-Rammahi (2012) made an analytical and experimental study of convection in cylinder occupied by metal foam. A metallic foam was also studied by Ando et al. (2013), Zhang et al. (2014), Rossi di Schio (2012), and (for periodic convection) by Rossi di Schio and Barletta (2012). Chen and Tsao (2012a) performed a thermal resistance analysis of forced convection with viscous dissipation using an entransy dissipation concept. (It should be noted that the novelty and utility of this concept have been questioned; see, for example, the discussion by Herwig (2014), Bejan (2014), Awad (2014), and Chen et al. (2014a, b, c).) The effect of radiation was included by Mahmoudi (2014), while Mahmoudi (2015) studied microchannels with internal heating and Mahmoudi and Karimi (2014) numerically investigated a partly filled pipe. The effect of radiation was also studied by Wang et al. (2014a, 2015b). A power law fluid was examined by Thayalan and Hung (2013). A channel with permeable walls was investigated by Rassoulinejad-Mousavi et al. (2014). Flow through an annulus was studied by Yang et al. (2011b).

LTNE was treated via a hyperbolic heat conduction model by Khadrawi et al. (2010). Some exact solutions for LTNE based on an effective porosity were obtained by Kuwahara et al. (2011). Chen et al. (2013a) treated numerically a metal foam layer in a horizontal channel with multiple discrete sources.

An analytical study of LTNE in tube heat exchangers was made by Dehghan et al. (2014a). A perturbation analysis of the LTNE condition in a porous medium bounded by an isothermal channel was made by Dehghan et al. (2014b). Abedou and Blouhadef (2015) have compared the practical usefulness of two LTNE criteria. The effect of anisotropic permeability on heat transfer through a porous river bed underlying a fluid layer was studied by Yovogan and Degan (2013). Wang et al. (2014a, b, c) made a numerical study of convection in ordered three-dimensional media. Abdollahzadeh Jamalabadi (2015) studied the effects of micro- and macro-scale viscous dissipation on thermally developing forced convection. Heat exchange in a porous channel with heat generation was investigated by Abedou et al. (2015). Chee et al. (2015) studied entropy generation in a channel with asymmetric thermal boundary conditions. Wang et al. (2015a, b, c) obtained an exact analytical solution for gaseous slip flow in a circular microtube. Xu et al. (2016) treated analytically slip flow through microfoams in mini/microchannels with asymmetric wall heat fluxes. Khademi (2016) made a detailed examination of forced convection in microchannels where the effect of thermal radiation from the solid phase is taken into account. Note that this paper was retracted because of plagiarism. Buonomo et al. (2016b) studied convection in microchannels with

viscous dissipation. Tajik Jamal-Abad et al. (2016) applied an LTNE model to a channel partly filled with porous material. Abedou et al. (2016) investigated convection in a self-heating channel.

4.11 Partly Porous Configurations

For complicated geometries numerical studies are needed. The use of porous bodies to enhance heat exchange motivated the early studies of Koh and Colony (1974) and Koh and Stevans (1975). Huang and Vafai (1993, 1994a, b, c, d) and Vafai and Huang (1994), using a Brinkman–Forchheimer model, performed studies of a composite system made of multiple porous blocks adjacent to an external wall (either protruding or embedded) or along a wall with a surface substrate. Khanafer and Vafai (2001, 2005) investigated isothermal surface production and regulation for high heat flux applications using porous inserts. Cui et al. (2000) conducted an experimental study involving a channel with discrete heat sources. A linear array of blocks in open and porous channels was studied by Rizk and Kleinstreuer (1991).

Convection in a parallel-plate channel partially filled with a porous layer was studied by Jang and Chen (1992). They found that the Nusselt number is sensitive to the open space ratio and that the Nusselt number is a minimum at a certain porous layer thickness, dependent on Darcy number. A similar study was reported by Tong et al. (1993). Srinivasan et al. (1994) analyzed convection in a spirally fluted tube using a porous substrate approach. Hadim and Bethancourt (1995) simulated convection in a channel partly filled with a porous medium and with discrete heat sources on one wall. Chikh et al. (1995b, 1998) studied convection in an annulus partly filled with porous material on the inner heated wall and in a channel with intermittent heated porous disks, while Rachedi and Chikh (2001) studied a similar problem. Ould-Amer et al. (1998) studied numerically the cooling of heat-generating blocks mounted on a wall in a parallel-plate channel. Fu et al. (1996) and Fu and Chen (2002) dealt with the case of a single porous block on a heated wall in a channel. Sözen and Kuzay (1996) studied round tubes with porous inserts. Zhang and Zhao (2000) treated a porous block behind a step in a channel. Masuoka et al. (2004) studied experimentally and numerically, with alternative interface conditions considered, the case of a permeable cylinder placed in a wind tunnel of rectangular cross section. Layeghi and Nouri-Borujerdi (2004) discussed forced convection from a cylinder or an array of cylinders in the presence or absence of a porous medium. Huang et al. (2004b) studied numerically the enhancement of heat transfer from multiple heated blocks in a channel using porous covers.

Abu-Hijleh (1997, 2000, 2001b, 2002) numerically simulated forced convection in various geometries with orthotropic porous inserts, while Abu-Hijleh (2003) treated a cylinder with permeable fins. A transient problem involving partly filled channels was studied by Abu-Hijleh and Al-Nimr (2001).

Analytical solutions for some flows through channels with composite materials were obtained by Al-Hadrami et al. (2001a, b). Pipes with porous substrates were

treated numerically by Alkam and Al-Nimr (1999a, b, 2001), while parallel-plate channels were similarly treated by Alkam et al. (2001, 2002). A tubeless solar collector and an unsteady problem involving an annulus were likewise treated by Al-Nimr and Alkam (1997a, 1998a). Hamdan et al. (2000) treated a parallel-plate channel with a porous core. Kim et al. (2003c) studied both a porous core and a porous sheath in a circular pipe. A Green's function method was used by Al-Nimr and Alkam (1998b) to obtain analytical solution for transient flows in parallel-plate channel. Experimental and numerical investigations of forced convection in channels containing obstacles were conducted by Young and Vafai (1998, 1999) and Pavel and Mohamad (2004a, b, c). An analytical solution for the case of an annulus was found by Qu et al. (2012b). A numerical simulation for turbulent flow in a channel was reported by Nimvari et al. (2012).

The limitation of the single-domain approach for the computation of convection in composite channels was exposed by Kuznetsov and Xiong (1999), following on from the work of Kuznetsov (1997e). The effect of thermal dispersion in a channel was analyzed by Kuznetsov (2001). Kuznetsov and Xiong (2000) numerically simulated the effect of thermal dispersion in a composite circular duct.

Kuznetsov (2000a) reviewed a number of analytical studies, including those by Kuznetsov (1998b, 1999a, c, 2001) for flow induced by pressure gradients, and by Kuznetsov (1998d, 2000b) and Xiong and Kuznetsov (2000) for Couette flow. The effect of turbulence on forced convection in a composite tube was discussed by Kuznetsov et al. (2002, 2003b), Kuznetsov (2004a), and Kuznetsov and Becker (2004). A numerical study of turbulent heat transfer above a porous wall was conducted by Stalio et al. (2004). Convection past a circular cylinder sheathed with a porous annulus, placed perpendicular to a turbulent air flow, was studied numerically and experimentally by Sobera et al. (2003). Hydrodynamically and thermally developing convection in a partly filled square duct was studied numerically using the Brinkman model by Jen and Yan (2005). The effects of a transition layer on forced convection in a channel were studied by Kuznetsov and Nield (2008a). They obtained an analytical solution involving a novel type of Airy function. Chen et al. (2008d) performed a numerical analysis based on stress-jump boundary conditions of flow past a porous square cylinder. Nield and Kuznetsov (2005d) studied the thermal development of flow in partly occupied channel or duct. Multi-plate porous insulation was studied by Lim et al. (2007). Combined convection and radiation in the entry region of circular ducts was studied by Chen and Sutton (2005). An analytical investigation of the effect of viscous dissipation on Couette flow in a channel partly occupied by a porous medium was carried out by Ghazian et al. (2011). A two-equation model was applied to tubes partly filled with metallic foam by Xu et al. (2011a, b). Umavathi et al. (2006, 2009) investigated oscillatory flow in a horizontal composite channel. Umavathi et al. (2010) studied generalized Couette flow in a composite channel.

A boundary-layer analysis of unconfined forced convection with a plate and a porous substrate was presented by Nield and Kuznetsov (2003d). A more general analytical investigation of this situation had been presented earlier by Kuznetsov

(1999b). The same problem for a wedge was treated by Kuznetsov and Nield (2006a).

Further general studies have been made by Mohais and Bhatt (2009), Huang et al. (2010), Sousa (2005), Yucel and Guven (2007, 2008), Yuan et al. (2008), Zahi et al. (2008), Zehforoosh and Hossainpour (2010), Bhargavi et al. (2009), Krishna (2009), Yang et al. (2009a), Satyamurty and Bhargavi (2010), Bhargavi and Satyamurty (2011), Shokoumand and Sayehvand (2010), Shokouhamand et al. (2011), Maerefat et al. (2011), Aguiilar-Madera et al. (2011a, b), Teamah et al. (2011a, b), Delavar and Hedayatpour (2012), Ucar et al. (2013a), and Cekmer et al. (2016). Turbulent flow has been further studied by Santos and de Lemos (2006), Allouache and Chikh (2008), Saati and Mohamad (2007), and Yang and Hwang (2008). Further studies with porous blocks were conducted by Hooman and Merrikh (2010), Li et al. (2010a), Shuja et al. (2009a, b), Tzesng (2006), and Tzeng et al. (2007). More work on fins or pins has been conducted by Do et al. (2007), Hamdan and Al-Nimr (2010), and Yang et al. (2010b). The case of a centered porous layer was studied by Cekmer et al. (2012). A variable section axisymmetric channel was treated by Pilevne and Misirlioglu (2007). A channel or an annulus partly filled with metallic foams was considered by Xu et al. (2011a, b) and Qu et al. (2012a). Entropy generation in pipes was studied by Mandavi et al. (2014). Heated oscillating plates were studied by Panda et al. (2013). An assessment of local thermal equilibrium in tubes with a porous core or sheath was made by Yang et al. (2012a) extending the work of Yang et al. (2009a). An exact solution with LTNE in a channel was reported by Karimi et al. (2014), while Mahmoudi and Maerefat (2011) also studied LTNE in a partly filled channel. A similar study was made by Xu et al. (2011a, b, c) for a tube and a parallel-plate channel. Also for a channel, Mahmoudi et al. (2014) examined the effect of various LTNE boundary conditions and Torabi et al. (2015a, b) included entropy generation with an LTNE model and with an internal source. A Lattice Boltzmann method was applied by Nazari et al. (2013a) to a channel partly filled with a porous block.

Non-Newtonian fluid flow in plane channels with porous blocks was studied by Nebbali and Bouhadef (2011). An analytical study of the effect of viscous dissipation in Couette flow in a partly filled channel was made by Ghazian et al. (2011). Experiments in all metallic wire-woven bulk Kagone sandwich panels were made by Joo et al. (2011). Valipour and Ghadi (2012) investigated numerically forced convective heat transfer around and through a porous circular cylinder with internal heat generation. Rashidi et al. (2013) studied convection round a solid cylinder wrapped with a porous ring. Rashidi et al. (2015c) compared numerically the use of stress-jump and stress-continuity interface conditions for flow across a solid cylinder with a porous sheath. Chaudhary and Kumar (2014) studied MHD boundary layer flow in an inclined anisotropic and heterogeneous layer. Karimi et al. (2015) examined the effects of exothermicity and endothermicity upon the temperature field in a partly filled channel. Dehghan (2015) studied the effects of heat generation on the thermal response of partly filled channels. Forchheimer forced convection in a rectangular channel partly filled with aluminum foam was investigated by Sener et al. (2016). Tajik Jamal-Abad et al. (2016) applied an LTNE model to a channel

partly filled with porous material. Lu et al. (2016b) reported an analytical solution for a parallel-plate channel partly filled with metallic foam. Wang et al. (2016a) studied gaseous slip flow through a parallel-plate channel with a centered porous substrate.

4.12 Transversely Heterogeneous Channels and Pipes

Kuznetsov (2000a) reviewed a number of analytical studies, including Kuznetsov (2000b) and Xiong and Kuznetsov (2000) for Couette flow. The effect of turbulence on forced convection in a composite tube was discussed by Kuznetsov et al. (2002, 2003b), Kuznetsov (2004a), and Kuznetsov and Becker (2004). A numerical study of turbulent heat transfer above a porous wall was conducted by Stalio et al. (2004). Convection past a circular cylinder sheathed with a porous annulus, placed perpendicular to a turbulent air flow, was studied numerically and experimentally by Sobera et al. (2003). Hydrodynamically and thermally developing convection in a partly filled square duct was studied numerically using the Brinkman model by Jen and Yan (2005). Chen et al. (2008d) performed a numerical analysis based on stress-jump boundary conditions of flow past a porous square cylinder. Nield and Kuznetsov (2005d) studied the thermal development of flow in partly occupied channel or duct. Multi-plate porous insulation was studied by Lim et al. (2007). Combined convection and radiation in the entry region of circular ducts was studied by Chen and Sutton (2005). An analytical investigation of the effect of viscous dissipation on Couette flow in a channel partly occupied by a porous medium was carried out by Ghazian et al. (2011). A two-equation model was applied to tubes partly filled with metallic foam by Xu et al. (2011a). Umavathi et al. (2010) studied generalized Couette flow in a composite channel.

A boundary-layer analysis of unconfined forced convection with a plate and a porous substrate was presented by Nield and Kuznetsov (2003d). A more general analytical investigation of this situation had been presented earlier by Kuznetsov (1999b). The same problem for a wedge was treated by Kuznetsov and Nield (2006a).

Further general studies have been made by Mohais and Bhatt (2009), Huang et al. (2010), Sousa (2005), Yucel and Guven (2007, 2008), Yuan and Chung (2008), Zahi et al. (2008), Zehforoosh and Hossainpour (2010), Bhargavi et al. (2009), Satyamurty and Bhargavi (2010), Bhargavi and Satyamurty (2011), Shokoumand and Sayehvand (2010), Maerefat et al. (2011), Aguiilar-Madera et al. (2011a, b), Teamah et al. (2011a, b), Turbulent flow has been further studied by Santos and de Lemos (2006), Allouache and Chikh (2008), Saati and Mohamad (2007), and Yang and Hwang (2008). Further studies with porous blocks were conducted by Hooman and Merrikh (2010), Li et al. (2010a), Shuja et al. (2009a, b), Tzeng (2006), and Tzeng et al. (2007). More work on fins or pins has been conducted by Do et al. (2007), Hamdan and Al-Nimr (2010), and Yang et al. (2010b).

Analytical studies on the effect on forced convection, in channels and ducts, of the variation in the transverse direction of permeability and thermal conductivity

were initiated by Nield and Kuznetsov (2000), who used the Darcy model for local thermal equilibrium. Both parallel-plate channels and circular ducts were considered, and walls at uniform temperature and uniform heat flux, applied symmetrically, were treated in turn. Both continuous variation and stepwise variation of permeability and conductivity were treated. For the parallel-plate channel, this work was extended to the Brinkman model by Nield and Kuznetsov (2003d). For the case of a parallel-plate channel with uniform heat flux boundaries, Sundaravadivelu and Tso (2003) extended the basic analysis to allow for the effect of viscosity variations. Asymmetric property variation and asymmetric heating in a parallel-plate channel were considered by Nield and Kuznetsov (2001a). A conjugate problem, with either a parallel-plate channel or a circular duct, was treated by Kuznetsov and Nield (2001). The interaction of thermal nonequilibrium and heterogeneous conductivity was studied by Nield and Kuznetsov (2001b). With application to the experimental results reported by Paek et al. (1999b) in mind, Nield and Kuznetsov (2003a) treated a case of gross heterogeneity and anisotropy using a layered medium analysis. A conjugate problem, involving the Brinkman model and with temperature-dependent volumetric heat inside the solid wall, was treated analytically and numerically by Mahmud and Fraser (2005). Nield and Kuznetsov (2013d) discussed arrangements of layers of given material to optimize the heat transfer. Ucar et al. (2013b) noted circumstances in which the Nusselt number changes sign. Jogie and Bhatts (2013) studied flow in a channel occupied by two immiscible fluids. Jamal-Abad et al. (2016) provided a perturbation solution to a problem with temperature-dependent conductivity.

For illustration, we present the results obtained by Nield and Kuznetsov (2000) for the effect of heterogeneity on Nusselt number. We first consider the case where the permeability and thermal conductivity distributions are given by

$$\begin{aligned} K &= K_0\left\{1+\varepsilon_{\mathrm{K}}\left(\frac{|y^*|}{H}-\frac{1}{2}\right)\right\},\\ k &= k_0\left\{1+\varepsilon_{\mathrm{k}}\left(\frac{|y^*|}{H}-\frac{1}{2}\right)\right\}. \end{aligned} \tag{4.134}$$

Here the boundaries are at $y^* = -H$ and $y^* = H$. The mean values of the permeability and conductivity are K_0 and k_0, respectively. The coefficients ε_{K} and ε_{k} are each assumed to be small compared with unity. To first order, one finds that for the case of uniform flux boundaries

$$\mathrm{Nu} = 6\left(1+\frac{1}{4}\varepsilon_{\mathrm{K}}-\frac{1}{8}\varepsilon_{\mathrm{k}}\right), \tag{4.135}$$

and for the case of uniform temperature boundaries,

$$\mathrm{Nu} = \frac{\pi^2}{2}\left\{1+\frac{2}{\pi^2}(\varepsilon_{\mathrm{K}}-\varepsilon_{\mathrm{k}})\right\}. \tag{4.136}$$

4.13 Thermal Development

In forced convection in a porous medium, hydrodynamic development is not normally of importance. This is because the hydrodynamic development length is readily shown to be of order of magnitude $(K/\varphi)^{1/2}$ and usually this is very small compared with the channel width. In contrast, the thermal development length can be much greater. An early study was that of Montakhab (1979), who considered a step change in inlet temperature.

For the Darcy model one has slug flow, and for the case of walls at uniform temperature the classical Graetz solution for thermal development is applicable. An analysis based on the Brinkman model was reported by Nield et al. (2004a), for both a parallel-plate channel and a circular tube. A finite-element numerical investigation was made by Misirlioglu (2007). The additional effect of a Forchheimer term has not yet been treated, but one would anticipate that since an increase in Forchheimer number would produce a more slug-like flow, the effect of quadratic drag would be similar to that produced by a reduction in Darcy number. The corresponding case where the walls are at uniform heat flux was treated by Nield et al. (2003b). The effect of local thermal nonequilibrium was examined by Nield et al. (2002), and the additional effects of transverse heterogeneity were studied by Nield and Kuznetsov (2004a, b, c). Thermal development in a channel occupied by a non-Newtonian power-law fluid was studied by Nield and Kuznetsov (2005a). In the standard analysis of the Graetz type the axial conduction and viscous dissipation effects are neglected, but in the studies by Nield et al. (2003a) and Kuznetsov et al. (2003c) these effects were included, for the cases of a parallel-plate channel and a circular duct, respectively. For the case of a circular duct, axial conduction effects and viscous dissipation effects were studied numerically by Hooman et al. (2003) and Ranjbar-Kani and Hooman (2004), respectively. A porous medium occupied by a rarefied gas was studied by Kuznetsov and Nield (2009b, 2010f). The case of local thermal nonequilibrium was examined by Yang and Liu (2006) and Dukhan (2009b), and thermal nonequilibrium, together with the effect of viscous dissipation, was studied by Chen and Tsao (2011c) (together with viscous dissipation). The effect of viscous dissipation was also studied by Hooman et al. (2006, 2007b) and Tada and Ichimiya (2007b). An entropy generation analysis was performed by Hooman (2005) and Hooman et al. (2008a).

A numerical study of heat transfer in the thermally developing region in an annulus was reported by Hsieh and Lu (1998). Thermally developing forced convection inside ducts of various shapes (including elliptical passages) was analyzed by Haji-Sheikh and Vafai (2004). Haji-Sheikh et al. (2005) illustrated the use of a combination of a Green's function solution and an extended weighted residuals method in the study of isosceles triangular passages. They noted that their methodology is equally applicable when the boundary conditions are of the first, second, or third kind. The effect of axial conduction in triangular ducts was studied by Banerjee et al. (2012). A field synergy principle analysis for the case of uniform heat generation was reported by Chen and Tsao (2012b). Ouyang et al. (2013b) and

Dehghan et al. (2016a) (analytically) considered the effect of local thermal nonequilibrium, while Dehghan et al. (2016d) added to LTNE the effect of internal heat generation.

Thermally developing forced convection in a metal foam-filled elliptical annulus was studied by Benmerkhi et al. (2016). An analytic investigation of convection through the entrance of a microchannel was reported by Dehghan et al. (2016c). Microchannels were further studied by Dehghan et al. (2016b).

The general feature of thermal development is that the Nusselt number increases as one moves from the fully developed region toward the entrance region. It is found that the rate of increase decreases as the Darcy number increases.

4.14 Surfaces Covered with Porous Layers

The hair growth on the skin of a mammal is an example of a saturated porous medium where, locally, the solid matrix (hair) is *not* in thermal equilibrium with the permeating fluid (air). A theory for the heat transfer by forced convection through a surface covered with hair has been developed by Bejan (1990a). It was tested subsequently in the numerical experiments of Lage and Bejan (1990). This entire body of work was reviewed by Bejan and Lage (1991) and Bejan (1992b).

The most essential features of the geometry of an actual surface covered with hair are retained in the model presented in Fig. 4.9. The skin surface is connected to a large number of perpendicular strands of hair, the density of which is assumed constant,

$$n = \frac{\text{number of strands of hair}}{\text{unit area of skin surface}}. \tag{4.137}$$

The hair population density n is related to the porosity of the "hair + air" medium that resides above the skin,

$$\varphi = \frac{\text{air volume}}{\text{total volume}} = 1 - nA_s. \tag{4.138}$$

Each strand of hair is modeled as a cylinder with the cross section A_s.

Parallel to the skin surface and through the porous structure formed by the parallel hair strands flows a uniform stream of air of velocity U. This stream is driven longitudinally by the dynamic pressure rise formed over that portion of the animal's body against which the ambient breeze stagnates. The longitudinal length L swept by the air flow is a measure of the linear size of the animal. The constant air velocity U is a quantity averaged over the volume occupied by air. It is assumed that the strand-to-strand distances are small enough so that the air flow behaves according to the Darcy law, with apparent slip at the skin surface.

At every point in the two-dimensional (x,y) space occupied by the porous medium described above, we distinguish two temperatures: the temperature of the

solid structure (the local hair strand), T_s, and the temperature of air that surrounds the strand, T_a. Both T_s and T_a are functions of x and y. The transfer of heat from the skin to the atmosphere is driven by the overall temperature difference $(T_w - T_\infty)$, where T_w is the skin temperature and T_∞ the uniform temperature of the ambient air that enters the porous structure. The temperature of the interstitial air, T_a, is equal to the constant temperature T_∞ in the entry plane $x = 0$.

For the solid structure, the appropriate energy equation is the classic conduction equation for a fin (in this case, single strand of hair),

$$k_s A_s \frac{\partial^2 T_s}{\partial y^2} - h p_s (T_s - T_a) = 0, \tag{4.139}$$

where p_s is the perimeter of a strand cross section. The thermal conductivity of the strand, k_s, and the perimeter-averaged heat transfer coefficient, h, are both constant. The constancy of h is a result of the assumed low Reynolds number of the air flow that seeps through the hair strands.

The second energy conservation statement refers to the air space alone, in which (ρc_P) and k_a are the heat capacity and thermal conductivity of air:

$$\rho c_P U \frac{\partial^2 T_a}{\partial x^2} = k_a \frac{\partial^2 T_a}{\partial y^2} + n h p_s (T_s - T_a). \tag{4.140}$$

On the left-hand side of this equation, we see only one convection term because the air-space-averaged velocity U points strictly in the x-direction. The first term on the right-hand side of the equation accounts for air conduction in the transversal direction (y). By not writing the longitudinal conduction term $k_a \, \partial^2 T_a / \partial x^2$, we are assuming that the flow region in which the effect of transversal air conduction is important is thin.

The last term in Eq. (4.140) accounts for the "volumetric heat source" effect that is due to the contact between the air stream and the local (warmer) hair strand. Note the multiplicative role of the strand density n in the makeup of this term: the product (np_s) represents the total contact area between hair and air, expressed per unit of air volume. The heat source term of Eq. (4.140) is the air-side reflection of the heat sink term (the second term) encountered in the fin conduction equation (4.139).

In an air region that is sufficiently close to the skin, the air stream is warmed up mainly by contact with the skin, i.e., not by the contact with the near-skin area of the hair strands. Consequently, for this region, in Eq. (4.140) the heat source term $nhp_s(T_s - T_a)$ can be neglected. On the other hand, sufficiently far from the skin most of the heating of the air stream is effected by the hair strands that impede the flow. In the energy balance of this external flow the vertical conduction term can be neglected in Eq. (4.140).

For the details of the heat transfer analysis of the two-temperature porous medium of Fig. 4.10 the reader is referred to the original paper (Bejan 1990a). One interesting conclusion is that the total heat transfer rate through a skin portion

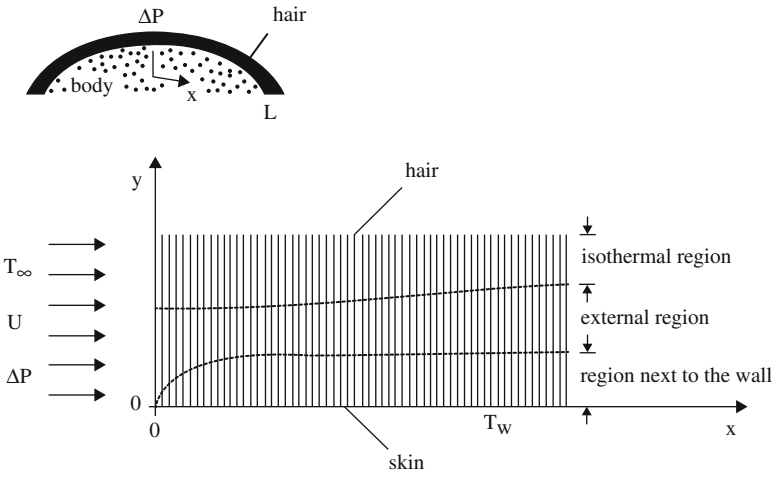

Fig. 4.10 Two-dimensional model for forced convection through the hair growth near the skin (after Bejan 1990a)

of length L is minimized when the hair strand diameter assumes the optimal value D_{opt} given by

$$\frac{D_{\text{opt}}}{\nu}\left(\frac{\Delta P}{\rho}\right)^{1/2} = \left(\frac{k_z^2 k_s}{2k_a}\right)^{1/4}\left(\frac{1-\varphi}{\varphi}\right)^{5/4}\left[\frac{L}{\nu}\left(\frac{\Delta P}{\rho}\right)^{1/2}\right]^{1/2}. \tag{4.141}$$

That lowest heat transfer rate is

$$\frac{q'_{\text{min}}}{k_a(T_w - T_\infty)} = \left(32\frac{k_s}{k_a}\right)^{1/4}\varphi^{3/4}(1-\varphi)^{1/4}\left[\frac{L}{\nu}\left(\frac{\Delta P}{\rho}\right)^{1/2}\right]^{1/2}. \tag{4.142}$$

These results are based on several additional assumptions, which include a model of type (1.5) for the permeability of the hair matrix

$$K \cong \frac{D^2\varphi^3}{k_z(1-\varphi)^2}, \tag{4.143}$$

where the constant k_z is a number of order 10^2.

Equation (4.142) shows that the minimum heat transfer rate increases with the square root of the linear size of the body covered with hair, $L^{1/2}$. The optimal hair strand diameter is also proportional to $L^{1/2}$. This last trend agrees qualitatively with measurements of the hair sizes of mammals compiled by Sokolov (1982). Figure 4.11 shows the natural hair strand diameters (D) of ten mammals, with the length scale of the body of the animal plotted on the abscissa.

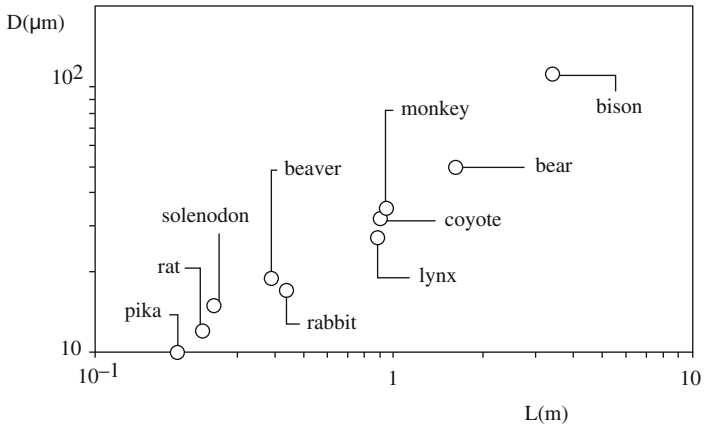

Fig. 4.11 The hair strand diameters and body lengths of ten mammals (Bejan and Lage 1991)

The natural design of animal body insulation is an important and visible manifestation of the constructal law of design in nature. Although many natural designs, animate and inanimate (e.g., river basins, lungs), speak loudly of the natural design tendency to facilitate flow access, the design of body insulation seems to contradict this tendency, because it opposes the flow of heat from body to ambient. In fact, there is no contradiction, because what flows in animal design is animal mass on the landscape, and the flow of animal mass is facilitated by all the detailed features of animal design, from the *minimization* of fluid flow resistance in lung architecture and vascularized tissues to the *maximization* of heat flow resistance in body insulation (Bejan and Lorente 2010, 2011, Bejan and Zane 2012).

Later studies of surfaces covered with fibers focused on the generation of reliable pressure drop and heat transfer information for low Reynolds number flow through a bundle of perpendicular or inclined cylindrical fibers (Fowler and Bejan 1994). There is a general need for data in the low Reynolds number range, as most of the existing results refer to heat exchanger applications (i.e., higher Reynolds numbers). Fowler and Bejan (1995) studied numerically the heat transfer from a surface covered with flexible fibers, which bend under the influence of the interstitial flow. Another study showed that when the effect of radiation is taken into account, it is possible to anticipate analytically the existence of an optimal packing density (or porosity) for minimal heat transfer across the porous cover (Bejan 1992b).

Vafai and Kim (1990) and Huang and Vafai (1993, 1994a, b, c, d) have shown that a porous coating can alter dramatically the friction and heat transfer characteristics of a surface. This effect was also documented by Fowler and Bejan (1995). Depending on its properties and dimensions, the porous layer can act either as an insulator or as a heat transfer augmentation device. The engineering value of this work is that it makes it possible to "design" porous coatings such that they control the performance of the solid substrate.

4.15 Designed Porous Media

A potentially revolutionary application of the formalism of forced convection in porous media is in the field of heat exchanger simulation and design. Heat exchangers are a century-old technology based on information and concepts stimulated by the development of large-scale devices (see, for example, Bejan 1993, Chap. 9). The modern emphasis on heat transfer augmentation, and the push toward miniaturization in the cooling of electronics, have led to the development of compact devices with much smaller features than in the past. These devices operate at lower Reynolds numbers, where their compactness and small dimensions ("pores") make them candidates for modeling as saturated porous media.

Such modeling promises to revolutionize the nomenclature and numerical simulation of the flow and heat transfer through heat exchangers. Decreasing dimensions, increasing compactness, and constructal design (Sect. 4.18) make these devices appear and function as *designed porous media* (Bejan 2004b; Lorente 2009). This emerging field is outlined in two new books (Bejan 2004a, b; Bejan et al. 2004).

To illustrate this change, consider Zukauskas' (1987) classical chart for the pressure drop in cross flow through arrays of staggered cylinders (e.g., Fig. 9.38 in Bejan 1993). The four curves drawn on this chart for the transverse pitch/cylinder diameter ratios 1.25, 1.5, 2, and 2.5 can be made to collapse into a single curve, as shown in Fig. 4.12 (Bejan and Morega 1993a, b). The technique consists of treating the bundle as a fluid-saturated porous medium and using the volume-averaged velocity U, the pore Reynolds number $UK^{1/2}/\nu$ on the abscissa, and the dimensionless pressure gradient group $(\Delta P/L)\, K^{1/2}/\rho U^2$ on the ordinate.

The effective permeability of the bundle of cylinders was estimated using Eq. (4.143) with $k_z = 100$, and Zukauskas' chart. Figure 4.12 shows very clearly the transition between Darcy flow (slope -1) and Forchheimer flow (slope 0). The porous medium presentation of the array of cylinders leads to a very tight collapse of the curves taken from Zukauskas' chart. The figure also shows the pressure drop curve for turbulent flow through a heat exchanger core formed by a stack of parallel plates. An added benefit of Fig. 4.12 is that it extends the curves reliably into the low Reynolds number limit (Darcy flow), where classic heat exchanger data are not available.

This method of presentation (Fig. 4.12) deserves to be extended to other heat exchanger geometries. Another reason for pursuing this direction is that the heat and fluid flow process can be simulated numerically more easily if the heat exchanger is replaced at every point by a porous medium with volume-averaged properties. An example is presented in Fig. 4.13 (Morega et al. 1995). Air flows from left to right along a hot horizontal surface (the electronics module) and through an array of parallel plate fins of rectangular profile (the heat sink). The plate thickness and plate-to-plate spacing are $t/L = 0.05$ and $d/L = 0.069$, where L is the length of the plate in the flow direction. The Reynolds number Re_L is based on L and the approach velocity. The air flows through and over the heat sink. The

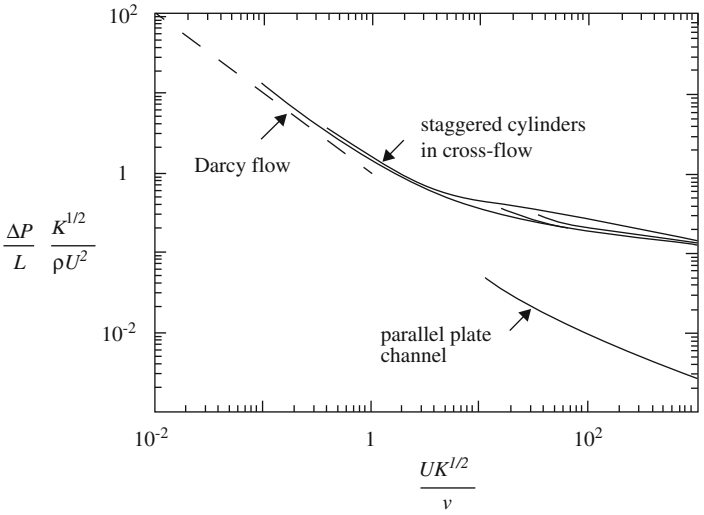

Fig. 4.12 Porous medium representation of the classic pressure-drop data for flow through staggered cylinders and stacks of parallel plates (Bejan and Morega 1993a, b)

corresponding temperature field and the effect of changing the Reynolds number are illustrated in Morega et al. (1995). One advantage of the numerical model is that it accounts in a volume-averaged sense for the conduction heat transfer through each plate, longitudinally and transversally. Another advantage comes from the relative simplicity and high computational speed, because in the thermal design and optimization of cooling techniques it is necessary to simulate a large number of geometric configurations such as Fig. 4.13.

Another important application of porous media concepts in engineering is in the optimization of the internal spacings of heat exchangers subjected to overall volume constraints (see Sects. 4.19 and 4.20). Packages of electronics cooled by forced convection are examples of heat exchangers that must function in fixed volumes. The design objective is to install as many components (i.e., heat generation rate) as possible, while the maximum temperature that occurs at a point (hot spot) inside the given volume does not exceed a specified limit. Bejan and Sciubba (1992) showed that a very basic trade-off exists with respect to the number of installed components, i.e., regarding the size of the pores through which the coolant flows. This trade-off is evident if we imagine the two extremes: numerous components (small pores) and few components (large spacings).

When the components and pores are numerous and small, the package functions as a heat-generating porous medium. When the installed heat generation rate is fixed, the hot spot temperature increases as the spacings become smaller, because in this limit the coolant flow is being shut off gradually. In the opposite limit, the hot spot temperature increases again because the heat transfer contact area decreases as the component size and spacing become larger. At the intersection of these two asymptotes we find an optimal spacing (pore size) where the hot spot temperature is

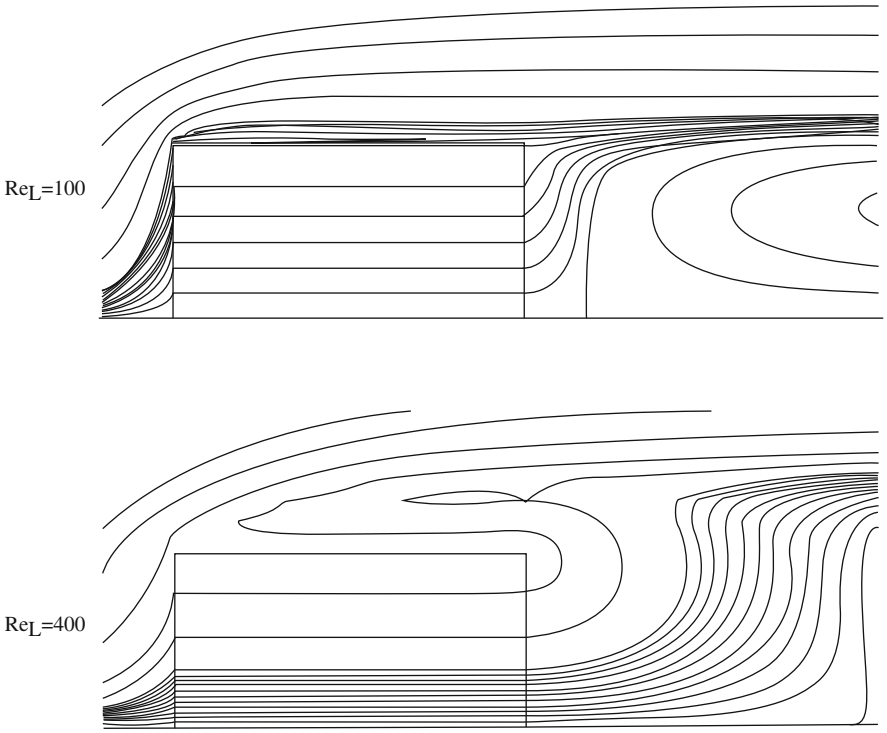

Fig. 4.13 The flow through and over a stack of rectangular parallel-plate fins attached to a base, and modeled as a porous medium (Morega et al. 1995)

minimal when the heat generation rate and volume are fixed. The same spacing represents the design with maximal heat generation rate and fixed hot spot temperature and volume. Bejan and Sciubba (1992), Bejan (1993), and Morega et al. (1995) developed analytical and numerical results for optimal spacings in applications with solid components shaped as parallel plates. Optimal spacings for cylinders in cross flow were determined analytically and experimentally by Bejan (1995) and Stanescu et al. (1996). The spacings of heat sinks with square pin fins and impinging flow were optimized numerically and experimentally by Ledezma et al. (1996). The latest conceptual developments are outlined in Sect. 4.19.

The dimensionless results developed for optimal spacings (S_{opt}) have generally the form

$$\frac{S_{opt}}{L} \sim \mathrm{Be}_L^{-n} \tag{4.144}$$

where L is the dimension of the given volume in the flow direction, and Be_L is the dimensionless pressure drop that Bhattacharjee and Grosshandler (1988) termed the Bejan number,

$$\mathrm{Be_L} = \frac{\Delta P \cdot L^2}{\mu_\mathrm{f} \alpha_\mathrm{f}}. \tag{4.145}$$

In this definition ΔP is the pressure difference maintained across the fixed volume. For example, the exponent n in Eq. (4.144) is equal to 1/4 in the case of laminar flow through stacks of parallel-plate channels. The Bejan number serves as the forced convection analog of the Rayleigh number used in natural convection (Petrescu 1994).

Designed porous media are now an active field of research in constructal theory and design. The progress on designed porous media was reviewed by Bejan and Lorente (2006, 2008, 2013).

The design of heat transfer processes in porous media is also an important new trend in the wider and rapidly growing field of thermodynamic optimization (Bejan 1996a). Noteworthy are two optimal-control papers of Kuznetsov (1997a, c), in which the heat transfer is maximized during the forced convection transient cooling of a saturated porous medium. For example, Kuznetsov (1997a) achieved heat transfer maximization by optimizing the initial temperature of the porous medium subject to a fixed amount of energy stored initially in the system and a fixed duration of the cooling process.

Progress on the design and performance of heat exchange structures with porous media was reported by Kamath et al. (2014), Adewumi et al. (2013), Kundu and Lee (2015), and Kephart and Jones (2016). Work on constructal design was surveyed in the book by Rocha (2009).

Alalaimi et al. (2015) developed analytically the formulas for effective permeability in several configurations using the closed-form description of tree networks designed to provide flow access. The objective was to find the relation between the permeability and porosity of tree-shaped fissures. They found the effect of the fracture size on the permeability for fixed number of bifurcation and the results showed that the permeability of the fracture network increased rapidly with the size of the fracture. The results have been validated by comparison with experimental and numerical results. The conclusion is that the permeability formulas do not vary much from one tree design to the next, suggesting that similar formulas may apply to naturally fissured porous media with unknown precise details, which occur in natural reservoirs.

4.16 Other Configurations or Effects

4.16.1 Effect of Temperature-Dependent Viscosity

The study of the effect of a temperature-dependent viscosity on forced convection in a parallel-plate channel was initiated by Nield et al. (1999). The original analysis was restricted to small changes of viscosity, carried out to first order in Nield et al.

(1999) and to second order in Narasimhan et al. (2001b), but the layered medium analysis of Nield and Kuznetsov (2003b) removed this restriction. For the case of a fluid whose viscosity decreases as the temperature increases (the usual situation) it is found that the effect of the variation is to reduce/increase the Nusselt number for cooled/heated walls. The analysis predicts that for the case of small Darcy number the effect of viscosity variation is almost independent of the Forchheimer number, while for the case of large Darcy number the effect of viscosity variation is reduced as the Forchheimer number increases. Within the limitations of the assumptions made in the theory, experimental verification was provided by Nield et al. (1999) and Narasimhan et al. (2001a).

For example, in the case of uniform flux boundaries and Darcy's law, Nield et al. (1999) showed that the mean velocity is altered by a factor $(1 + N/3)$ and the Nusselt number is altered by a factor $(1 - 2N/15)$, where the viscosity variation number N is defined as

$$N = \frac{q''H}{k}\frac{1}{\mu_0}\left(\frac{d\mu}{dT}\right)_0, \tag{4.146}$$

where the suffix 0 indicates evaluation at the reference temperature T_0.

The extension to the case where there is a substantial interaction between the temperature dependence of viscosity and the quadratic drag effect was carried out in a sequence of papers by Narasimhan and Lage (2001a, b, 2002, 2003, 2004a). The effect on pump power gain for channel flows was studied by Narasimhan and Lage (2004b). In these papers the authors developed what they call a Modified Hazen-Dupuit-Darcy model which they then validated with experiments with PAO as the convecting liquid and compressed aluminum-alloy porous foam as the porous matrix. This work on temperature-dependent viscosity was reviewed by Narasimhan and Lage (2005). Further studies on the effect of temperature-dependent viscosity were made by Hooman and Mohebpour (2007) and Hooman and Gurgenci (2008b). The variation of other thermophysical properties was studied by Pantokratoras (2007a, b).

The effects of a magnetic field and temperature-dependent viscosity on forced convection past a flat plate, with a variable wall temperature and in the presence of suction or blowing, were studied numerically by Seddeek (2002, 2005). Entropy generation studies were made by Hooman (2006), Hooman and Gurgenci (2007a), and Hooman et al. (2009a, b).The effect of temperature-dependent viscosity on thermally developing forced convection was studied by Hooman (2009a).

4.16.2 Oscillatory Flows, Counterflows

For an annulus and a pipe, Guo et al. (1997a, b) treated pulsating flow. For a completely filled channel, Kim et al. (1994) studied a pulsating flow numerically. Soundalgekhar et al. (Soundalgekar et al. 1991) studied flow between two parallel

plates, one stationary and the other oscillating in its own plane. Hadim (1994a) simulated convection in a channel with localized heat sources. A porous annulus was studied by Rashidi et al. (2014c) using a homotopy analysis method.

Sözen and Vafai (1991) analyzed compressible flow through a packed bed with the inlet temperature or pressure oscillating with time about a nonzero mean. They found that the oscillation had little effect on the heat storage capacity of the bed. Paek et al. (1999a) studied the transient cool down of a porous medium by a pulsating flow. Experiments involving steady and oscillating flows were conducted by Leong and Jin (2004, 2005). Reciprocating flows in channels partly filled with a porous medium were studied by Habibi et al. (2011).

An analytical treatment of pulsating flow in a channel or tube was presented by Kuznetsov and Nield (2006b). Pulsating convection from two heat sources mounted with porous blocks was examined by Huang and Yang (2008). Oscillatory flow of a non-Newtonian second grade fluid was studied by Hayat et al. (2007b). The effect of a periodically oscillating driving force on basic microflows was investigated by Haddad et al. (2006b). Dhahri et al. (2006a) studied pulsating flow in a tube partly filled with a porous medium, while Dhahri et al. (2006b) made a numerical study of reciprocating flow in a pipe. Khanafer et al.'s (2007) studied the influence of pulsatile blood flow on hyperthermia. MHD studies were reported by Mehmood et al. (2010) and Prasad et al. (2013a). Another flow involving flow oscillation was studied by Byun et al. (2006). Pulsatile flow of a Burger's fluid in a circular pipe was examined by El-Dabe et al. (2010).

Steady counterflow in a parallel-plate channel or a circular tube was studied by Nield and Kuznetsov (2008a) and Kuznetsov and Nield (2009a). The Nusselt number is zero when the net flow is zero. Pulsating counterflow in a channel with small amplitude fluctuations, without phase lag, was treated by Nield and Kuznetsov (2009a). A similar problem with phase lag was investigated by Nield and Kuznetsov (Nield and Kuznetsov 2010a, b, c, d, e). Pulsating counterflow in a circular tube was considered by Kuznetsov and Nield (2009b). Pathak and Ghiaasiaan (2010) considered the effect of thermal dispersion. Pathak et al. (2013) investigated a conjugate problem. Ghafarian et al. (2013) studied the case of metallic foam numerically. Dhahri et al. (2013a, b) treated viscous dissipation effect on entropy generation in cylindrical packed beds. Dhahri et al. (2008) studied entropy generation in a composite fluid/porous system.

Al-Sumaily and Thompson (2013) studied convection from a circular cylinder with pulsating flow, and Al-Sumaily et al. (2013) included the effect of local thermal nonequilibrium.

4.16.3 Non-Newtonian Fluids

Boundary-layer flow of a power-law fluid on an isothermal semi-infinite plate was studied by Wang and Tu (1989). The same problem for an elastic fluid of constant viscosity was treated by Shenoy (1992). These authors used a modified Darcy

model. A non-Darcy model for a power-law fluid was employed by Shenoy (1993a) and Hady and Ibrahim (1997) for flow past a flat plate, by Alkam et al. (1998) for flow in concentric annuli, and by Nakayama and Shenoy (1993b) and Chen and Hadim (1995, 1998a, b, 1999a) for flow in a channel. These studies showed that in the non-Darcy regime the effect of increase of power-law index n is to increase the thermal boundary-layer thickness and the wall temperature and to decrease the Nusselt number; in the Darcy regime the changes are small. As the Prandtl number increases, the Nusselt number increases, especially for shear-thinning fluids ($n < 1$). As n decreases, the pressure drop decreases. Tian et al. (2016) studied dissipation effects in a power-law fluid.

An elastic fluid was treated by Shenoy (1993b). A viscoelastic fluid flow over a nonisothermal stretching sheet was analyzed by Prasad et al. (2002). An experimental study for heat transfer to power-law fluids under flow with uniform heat flux boundary conditions was reported by Rao (2001, 2002).

A 3D flow in a duct was studied numerically by Nebbali and Bouhadef (2006). Flow over a flat plate of a power-law fluid in a Brinkman medium was analyzed by Pantokratoras and Magyari (2010). The effect of viscous dissipation on flow in a channel occupied by a power-law fluid was studied by Chen and Tsao (2011a). The effect of local thermal nonequilibrium in a channel lined with porous layers was examined by Abkar et al. (2010). Attia (2008b) studied the flow of a power-law fluid with a pressure gradient decaying exponentially with time. Wang et al. (2011) studied the case of a Gibson-Ashby constitutive model. Power-law slip flows and plug flows with variable thermophysical properties in parallel-plate and circular microchannels were investigated by Shojaeian and Kosar (2016).

Gokhale and Fernandez (2016) made a lattice Boltzmann simulation of forced convection in non-Newtonian fluid through a low permeable porous medium. Ramesh (2016) studied the effects of slip and convective conditions on the peristaltic flow of couple stress fluid in an asymmetric channel.

4.16.4 Bidisperse Porous Media

A bidisperse porous medium (BDPM) was introduced in Sect. 1.10.

Nield and Kuznetsov (2005b) treated forced convection in a parallel-plate channel occupied by a BDPM, using a two-temperature model similar to Eqs. (6.54) and (6.55) in this book. Nield and Kuznetsov (2004c) extended the analysis to the case of a conjugate problem with plane solid slabs bounding the channel. They found that the effect of the finite thermal resistance due to the slabs is to reduce both the heat transfer to the porous medium and the degree of local thermal nonequilibrium. An increase in the value of the Péclet number leads to decrease in the rate of exponential decay in the downstream direction, but does not affect the value of a suitably defined Nusselt number. The case of thermally developing convection in a BDPM was treated by Kuznetsov and Nield (2006c). The case of asymmetric heating of a channel was studied by Kuznetsov and Nield

(2010a). Heat transfer in a BDPM has been reviewed by Nield and Kuznetsov (2005c). A three-velocity three-temperature model of a tri-disperse porous medium was applied by Nield and Kuznetsov (2011b). Forced convection in a channel partly occupied by a bidisperse porous medium was studied by Nield and Kuznetsov (2011h). The hydrodynamic aspect of bidisperse porous media in the context of thermal management has been studied by Narasimhan et al. (2012). Nield and Kuznetsov (2013a, b, c, d, e, f, g, h) and Magyari (2013c) discussed the case of high speed flow. Straughan (2014a, b, c, d) studied bidispersive poroelastic waves. Hooman et al. (2015) reconsidered the modeling of momentum transfer. Grosan et al. (2010) studied flow through a spherical porous medium embedded in another porous medium.

Nield (2015a, b) proposed a more realistic model for a bidisperse porous medium. This model is based on consideration of unidirectional flow in a stack of channels with alternating fluid and porous phases, with the Beavers-Joseph boundary condition imposed at the interphase boundaries.

4.16.5 Other Flows, Other Effects

Non-Darcy boundary-layer flow over a wedge was studied using three numerical methods by Hossain et al. (1994). An application to the design of small nuclear reactors was discussed by Aithal et al. (1994). Convection with Darcy flow past a slender body was analyzed by Romero (1995b), while Sattar (1993) analyzed boundary-layer flow with large suction. The effect of blowing or suction on forced convection about a flat plate was also treated by Yih (1998d, e). The interaction with radiation in a boundary layer over a flat plate was studied by Mansour (1997). A porous medium heated by a permeable wall perpendicular to the flow direction was studied experimentally by Zhao and Song (2001). The boundary layer at a continuously moving surface was analyzed by Nakayama and Pop (1993) and Khan and Pop (2011a, b). The effect of liquid evaporation on forced convection was studied numerically by Shih and Huang (2002). A vertical wall with a convective thermal boundary condition was studied by Pantokratoras (2015).

Convection in an asymmetrically heated sintered porous channel was investigated by Hwang et al. (1995). Various types of sintered and un-sintered heat sinks were compared experimentally by Tzeng and Ma (2004). Convection in a sintered porous channel with inlet and outlet slots was studied numerically by Hadim and North (2005). Sung et al. (1995) investigated flow with an isolated heat source in a partly filled channel. Conjugate forced convection in cross flow over a cylinder array with volumetric heating in the cylinders was simulated by Wang and Georgiadis (1996). Heat transfer for flow perpendicular to arrays of cylinders was examined by Wang and Sangani (1997). An internally finned tube was treated as a porous medium by Shim et al. (2002). Internal heating has also been studied by Du and Wang (1999a, 2001) and Yang et al. (2009b). Forced convection in a system of wire screen meshes was examined experimentally by Ozdemir and Ozguc (1997).

The effect of anisotropy was examined experimentally by Yang and Lee (1999); numerically by Kim et al. (2001c), Nakayama et al. (2002), and Kim and Kuznetsov (2003); and analytically by Degan et al. (2002) and Sultani and Ajamein (2014). The effect of fins in a heat exchanger was studied numerically by Kim et al. (Kim et al. 2000a, b, 2002a, b, c) and by Kim and Hyun (2005). Forced convection in a channel with a localized heat source using fibrous materials was studied numerically by Angirasa and Peterson (1999). A numerical investigation with a random porosity model was made by Fu et al. (2001b). Experimental studies involving a rectangular duct heated only from the top wall were conducted by Demirel et al. (1999, 2000). A thermodynamic analysis of heat transfer in an asymmetrically heated annular packed bed was reported by Demirel and Kahraman (2000). A laboratory investigation of the cooling effect of a coarse rock layer and a fine rock layer in permafrost regions was reported by Yu et al. (2004). Forced convection in a rotating channel was examined experimentally by Tzeng et al. (2004) and analytically by Mohan and Srivastava (1978) (for a free channel bounded by a permeable bed). Experiments involving a confined slot jet were conducted by Jeng and Tzeng (2007a, b). Other experiments were performed by Noh et al. (2006), Tzeng (2007), Tzeng and Jeng (2006), Jeng et al. (2006, 2010), and Leong et al. (2010). Heat sinks involving nanofluids were studied by Ghazvini and Shokoumand (2009) and Ghazvini et al. (2009). The forced convection of nanofluids was also studied by Maghrebi et al. (2012).

Flow, thermal, and entropy generation characteristics inside a porous channel with viscous dissipation were discussed by Mahmud and Fraser (2005a, b). A similar problem with wavy enclosures filled with microstructures was studied by Mahmud et al. (2007). Further entropy studies were made by Abbasssi (2007), Hooman (2007), Hooman and Ejlali (2007), Hooman and Haji-Sheikh (2007), and Hooman et al. (2007a, 2008b). Other studies were made by Hooman (2008a), Hooman and Gorji-Bandpy (2006), Hooman and Merrikh (2006), Ichimiya et al. (2009), Jiang and Lu (2006, 2007), Lu et al. (2006), and Kamisli (2009). Dukhan and Hooman (2013) pointed out that the solution in Lu et al. (2006) is flawed because of an incorrect choice of Bessel function.

Forced convection in structured packed beds with spherical or ellipsoidal particles was studied computationally and experimentally by Yang et al. (2010a, c). Their results were compared with experimental data by Yang et al. (2012a, b, c, d, e). Hadad and Jafapur (2012, 2013) modeled packed beds with spherical pebbles of arbitrary shape. The effect of radiation in cylindrical packed beds was examined by Yee and Kamiuto (2005). The effect of radiation, with and without slip flow, was also studied by Dehghan et al. (2015a, b). Forced convection in parallel flow multilayer microchannels was treated by Saidi and Khiabani (2007). Flow through a channel with wire mesh packing was studied by Dyga (2010). The effect of viscous dissipation in an anisotropic channel with oblique principal axes was studied by Mobedi et al. (2010). A problem with heat generation was studied by Prakash et al. (2012a). Dehghan et al. (2015b, c) studied the effect of temperature-dependent conductivity and radiation in heat exchangers. Miguel and Heiter Reis (2005) studied transient convection in an isothermal porous layer. Mukhopadhyay et al. (2012) investigated

the effect of radiation on flow over a porous plate in a Darcy–Forchheimer porous medium. Rashidi et al. (2014d) simulated convection past a square diamond-shaped porous cylinder. Wang (2011a) studied flow through a polygonal duct. A numerical study of heat transfer in ordered three-dimensional porous media was reported by Wang et al. (2014b). Al-Sumaily (2014) studied convection from a bank of circular cylinders embedded in a porous medium. A discretely heated convergent channel was studied by Ghorab (2015a, b). Umavathi and Shekar (2014) studied the flow of a micropolar fluid induced by symmetric injection through parallel permeable disks. The influence of permeability on unsteady conjugate convection from a porous sphere embedded in a porous medium was investigated by Juncu (2014). Convection in a helical microchannel was treated by Narrein et al. (2015). The effect of rotation about a parallel axis on developing flow, in a rectangular channel or a partly filled square channel, was investigated by Alhusseny et al. (2015a, b). The effects of internal heat sources in porous channels with asymmetric thick walls were studied by Elliot et al. (2016). Mansour and Dawood (2016) studied numerically forced convection in wavy channels. Sayehvand et al. (2016) investigated convection from two cylinders placed in tandem.

A general study of forced convection from a thermodynamics perspective, with a focus on entropy generation, starting with the pore scale, for the Darcy and Forchheimer regimes, was reported by Torabi et al. (2016b).

The effects of a magnetic field have been studied by Filippov (1976), Chamkha (2001b), Eldabe and Sallam (2005a, b), Hayat and Abbas (2008) (second grade fluid), Rashad and Bakeir (2009), Saidu et al. (2010), Singh (2011a, b), Kumar and Gupta (2011), Kaya and Aydin (2012), Attia et al. (2012), Raju et al. (2013), Bakar et al. (2014), Vyas and Ranjan (2015), Ibanez (2015), and Srinivasacharya and Bindu (2016) (porous annulus, micropolar fluid). Sharma et al. (2016a, b) reported an entropy analysis of MHD forced convective flow through a circular channel in the presence of thermal radiation. Torabi and Peterson (2016) examined the effects of velocity slip and temperature jump on the heat transfer and entropy generation in microporous channels under a magnetic field. Rabhi et al. (2016) considered entropy generation, magnetic field, a microduct and local thermal non-equilibrium.

Sehat et al. (2014) and Sadrhosseini et al. (2016) reported an experimental study with a ferrofluid in a channel or tube. Sheikhnejad et al. (2015) studied convection in a ferrofluid in a partly filled horizontal tube.

4.17 Heatlines for Visualizing Convection

The concepts of heatfunction and heatlines were introduced for the purpose of visualizing the true path of the flow of energy through a convective medium (Kimura and Bejan 1983; Bejan 1984). The heatfunction accounts simultaneously for the transfer of heat by conduction and convection at every point in the medium. The heatlines are a generalization of the flux lines used routinely in the field of conduction. The concept of heatfunction is a spatial generalization of the concept of

Nusselt number, i.e., a way of indicating the magnitude of the heat transfer rate through any unit surface drawn through any point on the convective medium.

The heatline method was extended to several configurations of convection through fluid-saturated porous media (Morega and Bejan 1994). To illustrate the method, consider the uniform flow with thermal boundary layer, which is shown in Fig. 4.1. The heatfunction $H(x,y)$ is defined such that it satisfies identically the energy equation for the thermal boundary layer, Eq. (4.3). The H definition is in this case

$$\frac{\partial H}{\partial y} = (\rho c_P) u (T - T_{ref}), \tag{4.147}$$

$$-\frac{\partial H}{\partial x} = (\rho c_P) v (T - T_{ref}) - k_m \frac{\partial T}{\partial y}, \tag{4.148}$$

where the reference temperature T_{ref} is a constant. The flow field (u, v) and the temperature field (T) are furnished by the solutions to the convective heat transfer problem. It was pointed out in Trevisan and Bejan (1987a) that T_{ref} can have any value and that a heatline pattern can be drawn for each T_{ref} value. The most instructive pattern is obtained when T_{ref} is set equal to the lowest temperature that occurs in the convective medium that is being visualized. This choice was made in the construction of Figs. 4.14 and 4.15. In both cases the heatfunction can be obtained analytically. When the wall is colder (T_w) than the approaching flow (T_∞), (Fig. 4.14), the nondimensionalized heatfunction is

$$\widetilde{H}(\widetilde{x},\widetilde{y}) = \widetilde{x}^{1/2}\left[\eta \operatorname{erf}\left(\frac{\eta}{2}\right) + \frac{2}{\pi^{1/2}} \exp\left(-\frac{\eta^2}{4}\right)\right], \tag{4.149}$$

where $\widetilde{H} = H/\left[k_m (T_\infty - T_w) \mathrm{Pe}_l^{1/2}\right.$, $\mathrm{Pe}_L = U_\infty L/\alpha_m, \widetilde{x} = x/L$, and $\eta = y(U_\infty/\alpha_m x)^{1/2}$. In these expressions L is the length of the $y = 0$ boundary.

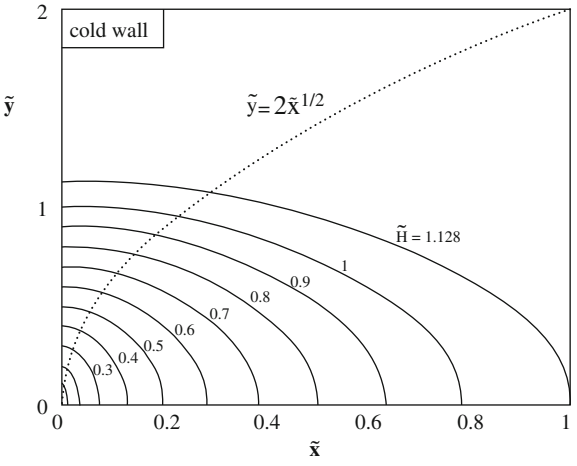

Fig. 4.14 The heatlines of the boundary layer near a cold isothermal wall (Morega and Bejan 1994)

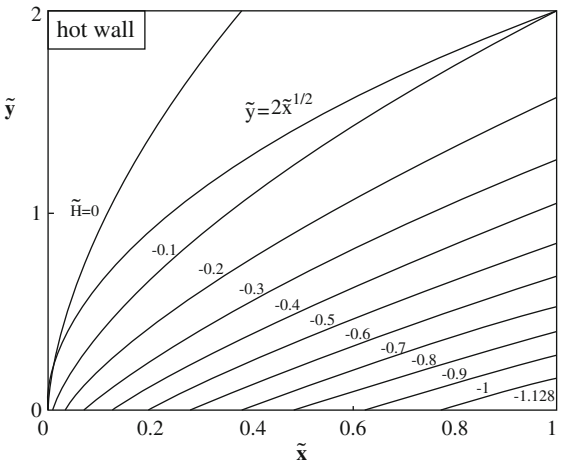

Fig. 4.15 The heatlines of the boundary layer near a hot isothermal wall (Morega and Bejan 1994)

Figure 4.14 shows that the H = constant curves visualize several features of convection near a cold wall. The energy that is eventually absorbed by the wall is brought into the boundary layer ($\widetilde{y} \cong 2\widetilde{x}^{1/2}$) by fluid from upstream of the cold section of the wall. The heatlines that enter the wall are denser near $\widetilde{x} = 0$, i.e., the heat flux is more intense. Finally, the value of the heatfunction increases along the wall, because the wall absorbs the heat released by the fluid. The trailing-edge $\widetilde{H}$ value matches the total heat transfer rate through the wall, Eq. (4.14).

Figure 4.15 shows the corresponding pattern of heatlines when the wall is warmer than the approaching fluid,

$$\widetilde{H}(\widetilde{x},\widetilde{y}) = \widetilde{x}^{1/2}\left[\eta \operatorname{erfc}\left(\frac{\eta}{2}\right) - \frac{2}{\pi^{1/2}}\exp\left(-\frac{\eta^2}{4}\right)\right]. \tag{4.150}$$

The heatlines come out of the wall at an angle because, unlike in Fig. 4.14, the gradient $\partial H/\partial y$ is not zero at the wall. Above the wall, the heatlines are bent even more by the flow because the effect of transversal conduction becomes weaker. The higher density of heatlines near $\widetilde{x} = 0$ indicates once again higher heat fluxes. The $\widetilde{H}$ value at the wall decreases in the downstream direction because the wall loses heat to the boundary layer.

Morega and Bejan (1994) displayed the heatlines for two additional configurations: boundary layers with uniform heat flux and flow through a porous layer held between parallel isothermal plates. As in Figs. 4.14 and 4.15, the heatlines for cold walls are unlike the heatlines for configurations with hot walls. In other words, unlike the patterns of isotherms that are used routinely in convection heat transfer (e.g., Fig. 7.4), the heatline patterns indicate the true direction of heat flow and distinguish between cold walls and hot walls.

Costa (2003) has reported a study of unified streamline, heatline, and massline methods of visualization of two-dimensional heat and mass transfer in anisotropic media. His illustrations include a problem involving natural convection in a porous medium.

Heatlines and masslines are now spreading throughout convection research as the proper way to visualize heat flow and mass flow. This method of visualization is particularly well suited for computational work and should be included in commercial computational packages. The growing activity based on the heatlines method was reviewed in Bejan (2004a) and Costa (2006a). The method is expanding vigorously, for example, in natural convection and mass transfer (Zhao et al. 2007a, b; Basak and Roy 2008; Dalal and Das 2008; Basak et al. 2009a, b; Singh et al. 2012), mixed convection (Roy et al. 2015), and porous media with nanofluid (Bondareva et al. 2016). The heatlines literature was reviewed most recently by Bejan (2015).

4.18 Constructal Tree Networks: Flow Access in Volume-to-Point Flow

It was discovered that by reducing systematically the thermal resistance between one point and a finite-size volume (an infinity of points) it is possible to predict a most common natural structure that previously was considered nondeterministic: the tree network (Bejan 1996b, 1997a, b; Ledezma et al. 1997). Tree network patterns abound in nature, in both animate and inanimate systems (e.g., botanical trees, lightning, neural dendrites, dendritic crystals). The key to solving this famous problem was the optimization of the shape of each finite-size element of the flow volume, such that the flow resistance of the element is minimal. The optimal structure of the flow—the tree network—then was *constructed* by putting together the shape-optimized building blocks. This construction of multiscale, hierarchical geometry became the starting point of the *constructal law* of design and evolution in Nature (Bejan 1997a, b, c, 2000, 2016; Bejan and Zane 2012).

The deterministic power of constructal theory is an invitation to new theoretical work on natural flow structures that have evaded determinism in the past. This section is about one such structure: the dendritic shape of the low-resistance channels that develop in natural fluid flows between a volume and one point in heterogeneous media (Bejan 1997b, c; Errera and Bejan 1999; Bejan et al. 2004). Examples of volume-to-point fluid flows are the bronchial trees, the capillary vessels, and the river drainage basins and deltas.

The deterministic approach outlined in this section is based on the proposition that a naturally occurring flow structure—its geometric form—is the end result of a process of geometric optimization. The objective of the optimization process is to construct the path (or assembly of paths) that provides minimal resistance to flow, or, in an isolated system, maximizes the rate of approach to equilibrium.

4.18.1 The Fundamental Volume-to-Point Flow Problem

Consider the fundamentals of evolutionary design toward less and less fluid flow resistance between one point and a finite-size volume (an infinity of points). For simplicity we assume that the volume is two-dimensional and represented by the area A (Fig. 4.16). The total mass flow rate $\dot{m}'$ (kg/sm) flows through the point M and reaches (or originates from) every point that belongs to A. We also assume that the volumetric mass flow rate $\dot{m}'''$ (kg/sm^3) that reaches all the points of A is distributed uniformly in space, hence $\dot{m}' = \dot{m}'''A$.

The space A is filled by a porous medium saturated with a single-phase fluid with constant properties. The flow is in the Darcy regime. If the permeability of the porous medium is uniform throughout A, then the pressure field $P(x, y)$ and the flow pattern can be determined uniquely by solving the Poisson-type problem associated with the point sink or point source configuration of Fig. 4.16. This classic problem is not the subject of this section.

Instead, we consider the more general situation where the space A is occupied by a nonhomogeneous porous medium composed of a material of low permeability K and a number of layers (e.g., cracks, filled or open) of much higher permeabilities (K_1, K_2, ...). The thicknesses (D_1, D_2, ...) and lengths (L_1, L_2, ...) of these layers are not specified.

For simplicity we assume that the volume fraction occupied by the high-permeability layers is small relative to the volume represented by the K material. There is a very large number of ways in which these layers can be sized, connected, and distributed in order to collect and channel $\dot{m}'$ to the point M. In other words, there are many designs of composite materials (K, K_1, K_2, ...) that can be installed in A: our objective is to find not only the internal architecture of the composite that minimizes the overall fluid flow resistance, but also a *strategy* for the geometric optimization of volume-to-point flows in general.

The approach we have chosen is illustrated in Fig. 4.16. We regard A as a patchwork of rectangular elements of several sizes (A_0, A_1, A_2, ...). We will show that the shape (aspect ratio) of each such element can be optimized

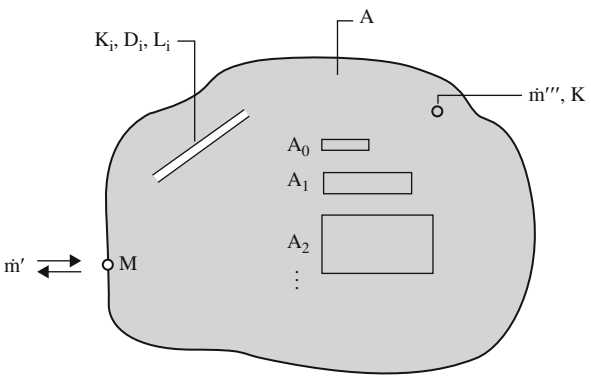

Fig. 4.16 The two-dimensional flow between one point (M) and a finite-size volume (A)

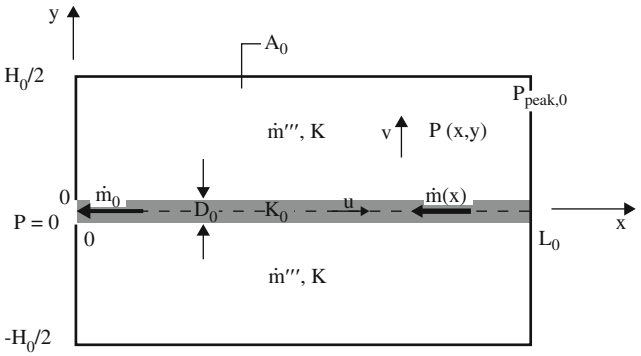

Fig. 4.17 The smallest volume element, with volumetric flow through the K porous medium and "channel" flow along a high-permeability layer (K_0)

for minimal flow resistance. The smallest element (A_0) contains only low-permeability material and one high-permeability layer (K_0, D_0) (Fig. 4.17). Each successively larger volume element (A_i) is an assembly of elements of the preceding size (A_{i-1}), which act as tributaries to the collecting layer (K_i, D_i, L_i) that defines the assembly. We will show that the optimally shaped assemblies can be arranged like building blocks to collect the volumetric flow $\dot{m}'''$ and transform it into the single stream $\dot{m}'$ at the point M.

Before presenting the analysis, it is worth commenting on the reasons for doing it and how it fits next to the vast amount of work that has been done in the same field. A general characteristic of the existing studies is that they begin with the often tacit assumption that a fluid tree network exists. Geometric details such as bifurcation (dichotomy) are assumed. No such assumptions are being made in this section. The problem solved in this section is the minimization of flow resistance between a finite-size volume and one point. The solution to this problem will show that certain portions of the optimized volume-to-point path are shaped as a tree network. In other words, unlike in the existing literature, in the present analysis the tree and its geometric details are results (predictions), not assumptions. This is a fundamental difference. It means that the solution to the volume-to-point flow problem sheds light on the universal design principle that serves as origin for the formation of fluid tree networks in nature.

4.18.2 The Elemental Volume

In Fig. 4.17 the smallest volume $A_0 = H_0 L_0$ is fixed, but its shape H_0/L_0 may vary. The flow, $\dot{m}'_0 = \dot{m}'''A_0$, A_0 is collected from the K medium by a layer of much higher permeability K_0 and thickness D_0. The flow is driven toward the origin (0, 0) by the pressure field $P(x, y)$. The rest of the rectangular boundary $H_0 \times L_0$ is

impermeable. Since the flow rate $\dot{m}'_0$ is fixed, to minimize the flow resistance means to minimize the peak pressure (P_{peak}) that occurs at a point inside A_0. The pressure at the origin is zero.

The analysis is greatly simplified by the assumptions that were mentioned already ($K \ll K_0$, $D_0 \ll H_0$), which, as we will show in Eq. (4.148), also mean that the optimized A_0 shape is such that H_0 is considerably smaller than L_0. According to these assumptions the flow through the K domain is practically parallel to the y direction,

$$P(x, y) \cong P(y) \quad \text{for} \quad H_0/2 > |y| > D_0/2 \tag{4.151}$$

while the flow through the K_0 layer is aligned with the layer itself $P(x, y) \cong P(x)$ for $|y| < D_0/2$. Symmetry and the requirement that P_{peak} be minimum dictate that the A_0 element has to be oriented such that the K_0 layer is aligned with the x axis. The mass flow rate through this layer is $\dot{m}'(x)$, with $\dot{m}'(0) = \dot{m}'_0$ at the origin (0, 0), and $\dot{m}'(L_0) = 0$. The K material is an isotropic porous medium with flow in the Darcy regime,

$$v = \frac{K}{\mu}\left(-\frac{\partial P}{\partial y}\right) \tag{4.152}$$

In this equation v is the volume-averaged velocity in the y direction (Fig. 4.17). The actual flow is oriented in the opposite direction. The pressure field $P(x, y)$ can be determined by eliminating v between Eq. (4.151) and the local mass continuity condition

$$\frac{\partial v}{\partial y} = \frac{\dot{m}'''}{\rho} \tag{4.153}$$

and applying the boundary conditions $\partial P/\partial y = 0$ at $y = H_0/2$ and $P = P(x, 0)$ at $y \cong 0$ (recall that $D_0 \ll H_0$):

$$P(x, y) = \frac{\dot{m}'''\nu}{2\mathrm{K}}\left(H_0 y - y^2\right) + P(x, 0). \tag{4.154}$$

Equation (4.154) holds only for $y \gtrsim 0$. The corresponding expression for $y \gtrsim 0$ is obtained by replacing H_0 with $-H_0$ in Eq. (4.154).

The pressure distribution in the K_0 material, namely $P(x,0)$, is obtained similarly by assuming Darcy flow along a D_0-thin path near $y = 0$,

$$u = \frac{K_0}{\mu}\left(-\frac{\partial P}{\partial x}\right), \tag{4.155}$$

where u is the average velocity in the x-direction. The flow proceeds toward the origin, as shown in Fig. 4.17. The mass flow rate channeled through the K_0 material is $\dot{m}'(x) = -rD_0u$. Furthermore, mass conservation requires that the

mass generated in the infinitesimal volume slice ($H_0\,dx$) contributes to the $\dot{m}'(x)$ stream: $\dot{m}'''H_0 dx = -d\dot{m}'$. Integrating this equation away from the impermeable plane $x = L_0$ (where $\dot{m}' = 0$), and recalling that $\dot{m}'_0 = \dot{m}'''H_0 L_0$, we obtain

$$\dot{m}\,(x) = \dot{m}'''H_0(L_0 - x) = \dot{m}_0\left(1 - \frac{x}{L_0}\right). \tag{4.156}$$

Combining these equations we find the pressure distribution along the x axis

$$P\,(x, 0) = \frac{\dot{m}'_0\nu}{D_0 K_0}\left(x - \frac{x^2}{2L_0}\right). \tag{4.157}$$

Equations (4.154) and (4.157) provide a complete description of the $P(x, y)$ field. The peak pressure occurs in the farthest corner ($x = L_0$, $y = H_0/2$):

$$P_{\text{peak},0} = \dot{m}'_0\nu\left(\frac{H_0}{8KL_0} + \frac{L_0}{2K_0 D_0}\right). \tag{4.158}$$

This pressure can be minimized with respect to the shape of the element (H_0/L_0) by noting that $L_0 = A_0/H_0$ and $\varphi_0 = D_0/H_0 \ll 1$. The number φ_0 is carried in the analysis as an unspecified parameter. For example, if the D_0 layer was originally a crack caused by the volumetric shrinking (e.g., cooling, drying) of the K medium, then D_0 must be proportional to the thickness H_0 of the K medium. The resulting geometric optimum is described by

$$\frac{H_0}{L_0} = 2\left(\widetilde{K}_0\varphi_0\right)^{-1/2} \qquad \widetilde{L}_0 = 2^{-1/2}\left(\widetilde{K}_0\varphi_0\right)^{1/4} \tag{4.159}$$

$$\widetilde{H}_0 = 2^{1/2}\left(\widetilde{K}_0\varphi_0\right)^{-1/4} \qquad \Delta\widetilde{P}_0 = \frac{1}{2}\left(\widetilde{K}_0\varphi_0\right)^{-1/2} \tag{4.160}$$

The nondimensionalization used in Eqs. (4.146) and (4.147) and retained throughout this section is based on using $A_0^{1/2}$ as length scale and K as permeability scale:

$$\left(\widetilde{H}_i, \widetilde{L}_i\right) = \frac{(H_i, L_i)}{A_0^{1/2}}, \qquad \widetilde{K}_i = \frac{K_i}{K}, \tag{4.161}$$

$$\Delta\widetilde{P}_i = \frac{P_{\text{peak},i}}{\dot{m}'''A_i\nu/K}, \qquad \varphi_i = \frac{D_i}{H_i}. \tag{4.162}$$

At the optimum, the two terms on the right side of Eq. (4.158) are equal. The shape of the A_0 element is such that the pressure drop due to flow through the K material is equal to the pressure drop due to the flow along the K_0 layer. Note also that the first of Eq. (4.160) confirms the assumptions made about the D_0 layer at the

start of this section: high permeability ($\widetilde{K}_0 >> 1$) and small volume fraction ($\varphi_0 \ll 1$) mean that the optimized A_0 shape is slender, $H_0 \ll L_0$, provided that $\widetilde{K}_0 >> \varphi_0^{-1}$.

4.18.3 The First Construct

Consider next the immediately larger volume $A_1 = H_1\, L_1$ (Fig. 4.18) which can contain only elements of the type optimized in the preceding section. The streams $\dot{m}'_0$ collected by the D_0-thin layers are now united into a larger stream $\dot{m}'_1$ that connects A_1 with the point $P = 0$. The $\dot{m}'_1$ stream is formed in the new layer (K_1, D_1, L_1).

The problem of optimizing the shape of the A_1 rectangle is the same as the A_0 problem that we just solved. First, we note that when the number of A_0 elements assembled into A_1 is large, the composite material of Fig. 4.18 is analogous to the composite of Fig. 4.17, provided that the permeability K of Fig. 4.17 is replaced by an equivalent (volume averaged) permeability (K_{e1}) in Fig. 4.18. The K_{e1} value is obtained by writing that the pressure drop across an A_0 element [Eq. (4.160)] is equal to the pressure drop over the distance $H_1/2$ in the K_{e1} medium [this second pressure drop can be read off Eq. (4.154), after replacing H_0 with H_1, y with $H_1/2$, and K with K_{e1}]. The result is $K_{e1} = K_0\, \varphi_0$: this value is then used in place of K_0, in an analysis that repeats the steps executed in Eqs. (4.158)–(4.160) for the A_0 optimization problem.

A clearer alternative to this analysis begins with the observation that the peak pressure ($P_{\text{peak}.1}$) in Fig. 4.18 is due to two contributions: the flow through the upper-right corner element ($P_{\text{peak}.0}$) and the flow along the (K_1, D_1) layer:

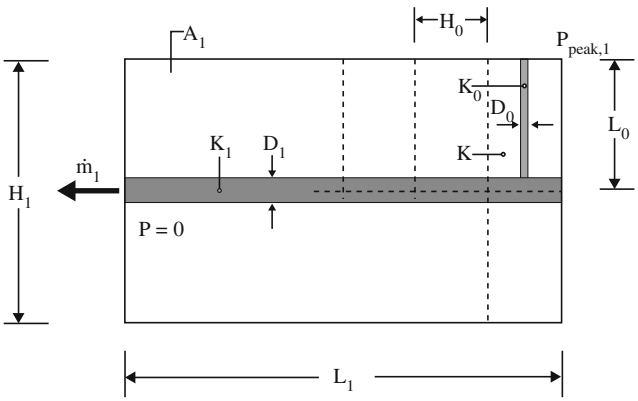

Fig. 4.18 The first assembly (A_1) of elements of size A_0, and the new high-permeability layer K_1

$$P_{\text{peak},1} = \dot{m}'''A_0 \frac{\nu}{K}\frac{1}{2}\left(\widetilde{K}_0\varphi_0\right)^{-1/2} + \dot{m}'_1\nu\frac{L_i}{2K_1D_1}. \tag{4.163}$$

This expression can be rearranged by using the first of Eqs. (4.160) and $H_1 = 2L_0$:

$$\frac{P_{\text{peak},1}}{\dot{m}'''A_1\nu/K} = \frac{1}{4\widetilde{K}_0\varphi_0}\frac{H_1}{L_1} + \frac{1}{2\widetilde{K}_1\varphi_1}\frac{L_1}{H_1}. \tag{4.164}$$

The corner pressure $P_{\text{peak},1}$ can be minimized by selecting the H_1/L_1 shape of the A_1 rectangle. The resulting expressions for the optimized geometry $(H_1/L_1, \widetilde{H}_1, \widetilde{L}_1)$ are listed in Table 4.1. The minimized peak pressure $\left(\Delta\widetilde{P}_1\right)$ is divided equally between the flow through the corner A_0 element and the flow along the collecting (K_1, D_1) layer. In other words, as in the case of the A_0 element, the geometric optimization of the A_1 assembly is ruled by a principle of *equipartition* of pressure drop between the two main paths of the assembly (Lewins 2003).

4.18.4 Higher-Order Constructs

The assembly and area shape optimization procedure can be repeated for larger assemblies $(A_2, A_3, \ldots)$. Each new assembly (A_i) contains a number (n_i) of assemblies of the immediately smaller size (A_{i-1}), the flow of which is collected by a new high-permeability layer (K_i, D_i, L_i). As in the drawing shown in Fig. 4.17 for A_1, it is assumed that the number of constituents n_i is sensibly larger than 2. The analysis begins with the statement that the maximum pressure difference sustained by A_i is equal to the pressure difference across the optimized constituent (A_{i-1}) that occupies the farthest corner of A_i, and the pressure drop along the K_i central layer:

$$P_{\text{peak},i} = P_{\text{peak},i-1} + \dot{m}'_i\nu\frac{L_i}{2K_iD_i}. \tag{4.165}$$

The geometric optimization results are summarized in Table 4.1, in which we used $C_i = \widetilde{K}_i\varphi_i$ for the dimensionless flow conductance of each layer. The optimal

Table 4.1 The optimized geometry of the elemental area A_0 and the subsequent assemblies when the channel permeabilities are unrestricted (Note: $C_i = K_i\varphi_i$)

i	H_i/L_i	$\widetilde{H}_i$	$\widetilde{L}_i$	$n_i = A_i/A_{i-1}$	$\Delta\widetilde{P}_i$
0	$2C_0^{-1/2}$	$2^{1/2}C_0^{-1/4}$	$2^{-1/2}C_0^{1/4}$	–	$\frac{1}{2}C_0^{-1/2}$
1	$(2C_0/C_1)^{1/2}$	$2^{1/2}C_0^{1/4}$	$C_0^{-1/4}C_1^{1/2}$	$(2C_1)^{1/2}$	$(2C_0C_1)^{-1/2}$
2	$(2C_1/C_2)^{1/2}$	$2C_0^{-1/4}C_1^{1/2}$	$2^{1/2}C_0^{-1/4}C_2^{1/2}$	$2(C_2/C_0)^{1/2}$	$(2C_1C_2)^{-1/2}$
$i \geq 2$	$(2C_{i-1}/C_i)^{1/2}$	$2^{i/2}C_0^{-1/4}C_{i-1}^{1/2}$	$2^{(i-1)/2}C_0^{-1/4}C_i^{1/2}$	$2(C_1/C_{i-2})^{1/2}$	$(2C_{i-1}C_i)^{-1/2}$

shape of each rectangle $H_i \times L_i$ is ruled by the pressure-drop equipartition principle noted in the optimization of the A_0 and A_1 shapes.

Beginning with the second assembly, the results fall into the pattern represented by the recurrence formulas listed for $i \geq 2$. If these formulas were to be repeated *ad infinitum* in both directions—toward large A_i and small A_i—then the pattern formed by the high-permeability paths (K_i, D_i) would be a fractal. Natural tree-shaped flows and those predicted by constructal theory are not fractal. In the present solution to the volume-to-point flow problem, the construction begins with an element of finite size, A_0, and ends when the given volume (A) is covered. Access to the infinity of points contained by the given volume is not made by making A_0 infinitely small. Instead, all the points of the given volume are reached by a diffusive flow that bathes A_0 *volumetrically*, because the permeability K of the material that fills A_0 is the lowest of all the permeabilities of the composite porous medium. Constructal theory is the clearest statement that the geometry of nature is not fractal (Bejan 1997c) and the first theory that predicts the multitude of natural flow structures that could be described as "fractal-like" structures (Poirier 2003; Rosa et al. 2004).

Figure 4.19 illustrates the minimal-resistance architecture recommended by the results of Table 4.1. At each level of assembly, the calculated number of constituents n_i was rounded off to the closest even number. The optimal design of the composite porous medium contains a tree network of high-permeability layers (K_0, K_1, K_2, ...), where the interstitial spaces are filled with low-permeability material (K). The actual shape of the tree depends on the relative size of the flow conductance parameters C_i. The conductance increase ratio C_i/C_{i-1} is essentially equal to

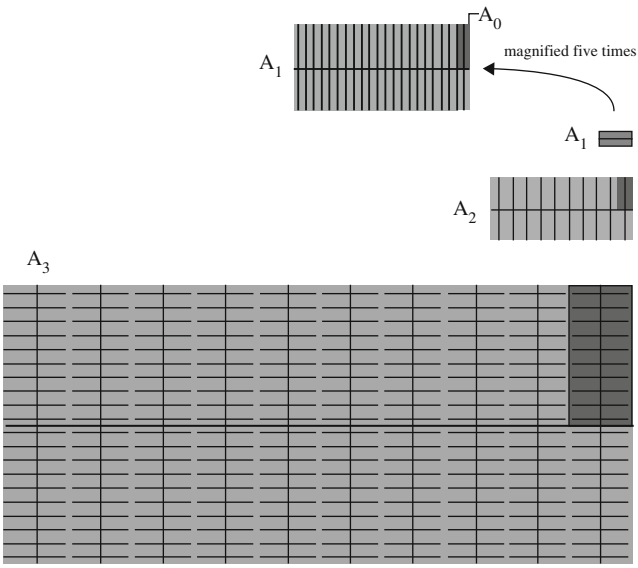

Fig. 4.19 Composite medium tree architecture for minimal volume-to-point flow resistance when $C_0 = 100$ and $C_i/C_i - 1 = 10$ for $i = 1, 2$, and 3

the permeability ratio K_i/K_{i-1}, because the volume fraction ($\varphi_i \ll 1$) is expected to vary little from one assembly to the next, cf. the comment made above Eq. (4.167). In other words, the conductance parameters C_i can be specified independently because the porousmedium characteristics of the materials that fill the high-permeability channels have not been specified.

Several trends are revealed by constructions such as Fig. 4.19. When the conductance ratio C_i/C_{i-1} is large, the number n_i is large, the optimal shape of each assembly is slender ($H_i/L_i < 1$), and the given volume is covered "fast," i.e., in a few large steps of assembly and optimization. When the ratio C_i/C_{i-1} is large but decreases from one assembly to the next, the number of constituents decreases and the shape of each new assembly becomes closer to square.

Combining the limit $C_i/C_{i-1} \to 1$ with the n_i formula of Table 4.1, we see that the number *two* (i.e., dichotomy, bifurcation, pairing) emerges as a result of geometric optimization of volume-to-point flow. Note that the actual value $n_i = 2$ is not in agreement with the $n_i > 2$ assumption that was made in Fig. 4.18 and the analysis that followed. This means that when $C_i/C_{i-1} \sim 1$ is of order 1, the analysis must be refined by using, for example, Fig. 4.18 in which the length of the (K_1, D_1) layer is not L_1 but $(n_1/2 - 1)H_0 + H_0/2$. In this new configuration the right-end tip of the (K_1, D_1) layer is absent because the flow rate through it would be zero. To illustrate this feature of the tree network, in Fig. 4.19 the zero-flow ends of the central layers of all the assemblies have been deleted.

4.18.5 *The Constructal Law of Design and Evolution in Nature*

The point-to-volume resistance can be minimized further by varying the angle between tributaries (D_{i-1}) and the main channel (D_i) of each new volume assembly. This optimization principle is well known in physiology where the work always begins with the assumption that a tree network of tubes *exists*. It can be shown numerically that the reductions in flow resistance obtained by optimizing the angles between channels are small relative to the reductions due to optimizing the shape of each volume element and assembly of elements. In this section we fixed the angles at 90° and focused on the optimization of volume shape. It is the optimization of shape subject to volume constraint—the consistent use of this principle at every volume scale—that is responsible for the emergence of a tree network between the volume and the point. We focused on the optimal shapes of building blocks because our objective was to discover a single optimization principle that can be used to explain the origin of tree-shaped networks in natural flow systems. The objective was to find the physics principle that was missing in the tree-like images generated by assumed fractal algorithms.

In summary, we solved in general terms the fundamental fluid mechanics problem of minimizing the flow resistance between one point and a finite-size

volume. A single optimization principle—the optimization of the shape of each volume element such that its flow resistance is minimized—is responsible for all the geometric features of the point-to-volume flow path. One of these features is the geometric structure—the tree network—formed by the portions with higher permeabilities ($K_0, K_1, \ldots$). The interstices of the network, i.e., the infinity of points of the given volume, are filled with material of the lowest permeability (K) and are touched by a flow that diffuses through the K material.

The most important conclusion is that the larger picture, the optimal overall performance, structure, and working mechanism can be described in a purely deterministic fashion; that is, if the resistance-minimization principle is recognized as law. This law can be stated as follows (Bejan 1996a, b, 1997a, 2016):

> For a finite-size system to persist in time (to live), it must evolve in such a way that it provides easier access (less resistance) to the imposed currents that flow through it.

This statement has two parts. First, it recognizes the natural tendency of imposed global currents to construct paths (shapes, structures) for better access through constrained open systems. The second part accounts for the evolution of the structure, which occurs in an identifiable direction that can be aligned with time itself. Small size and shapeless flow (diffusion) are followed in time by larger sizes and organized flows (streams). The optimized complexity continues to increase in time. Optimized complexity must not be confused with maximized complexity.

How important is the constructal approach to the minimal-resistance design, i.e., this single geometric optimization principle that allows us to anticipate the tree architecture seen in so many natural systems? In contemporary physics a significant research volume is being devoted to the search for universal design principles that may explain organization in animate and inanimate systems. In this search, the tree network is recognized as the symbol of the challenge that physicists and biologists face (Kauffman 1993, pp. 13 and 14): Imagine a set of identical round-topped hills, each subjected to rain. Each hill will develop a particular pattern of rivulets which branch and converge to drain the hill. Thus the particular branching pattern will be unique to each hill, a consequence of particular contingencies in rock placement, wind direction, and other factors. The particular history of the evolving patterns of rivulets will be unique to each hill. But viewed from above, the statistical features of the branching patterns may be very similar. Therefore, we might hope to develop a theory of the statistical features of such branching patterns, if not of the particular pattern on one hill.

The constructal approach outlined in this section is an answer to the challenge articulated so well by Kauffman. It introduces an engineering flavor in the current debate on natural organization, which until now has been carried out in physics and biology. By training, engineers begin the design of a device by first understanding its purposes. The size of the device is always finite, never infinitesimal. The device must function (i.e., fulfill its purpose) subject to certain constraints. Finally, to analyze (describe) the device is not sufficient: to optimize it, to construct it, and to make it work are the ultimate objective. All these features—purpose, finite size, constraints, optimization, and construction—can be seen in the network

constructions reported in this section. The resulting tree networks are entirely deterministic, and consequently they represent an alternative worthy of consideration in fields outside engineering. The progress in this direction is summarized in Bejan (1997c, 2000), Bejan and Lorente (2008, 2010, 2011), and Bejan and Zane (2012).

The short discussion here is confined to hydrodynamic aspects. For conduction, convection, turbulence, and other flows with structure, the reader is referred to the books that review the growing interest in constructal theory (Bejan 2000; Rosa et al. 2004; Bejan et al. 2004). For example, constructal trees were designed for chemically reactive porous media by Azoumah et al. (2004) and Zhou et al. (2008). The constructal law was used to predict the basic features and dimensions of Bénard convection and nucleate boiling (Nelson and Bejan 1998), the sand size and beachface slope (Reis and Gama 2010), and dust particle clusters (Reis et al. 2006).

The place of the constructal law as a self-standing law in thermodynamics is firmly established (Bejan and Lorente 2004). The constructal law is distinct from the second law. For example, with respect to the time evolution of an isolated thermodynamic system, the second law states that the system will proceed toward a state of equilibrium ("nothing moves," maximum entropy at constant energy). In this second-law description, the system is a black box, without configuration.

With regard to the same isolated system, the constructal law states that the currents that flow in order to bring the system to equilibrium will seek and develop paths of maximum access. In this way, the system develops its flow configuration, which endows the system with the ability to approach its equilibrium the fastest.

The constructal law is the law of design generation, whereas the second law is the law of entropy generation. The constructal law can be stated in several equivalent ways: a principle of flow access maximization (or efficiency increase), as in the original statement quoted above, a principle of flow compactness maximization (miniaturization), and a principle of flow territory maximization, as in the spreading of river deltas, living species, and empires (Bejan and Lorente 2004).

Applications of constructal design to the regenerators that operate cyclically in various types of heating or reheating furnaces were made by Bejan et al. (2013). A thermal analysis of a T-shaped porous fin with radiation effects was undertaken by Bhanja and Kundu (2013). Radial flow in a heterogeneous porous medium based on fractal and constructal tree networks was analyzed by Xu et al. (2008a, b).

Using constructal theory, Chen et al. (2014a, b, c, d) investigated flow in a porous medium with a "disk-point" mass transfer model. They modeled the mass flow using either the Darcy law or the Hagen-Poiseuille law. They obtained optimal constructs of radial-pattern and branched-pattern disks with minimization of the maximum pressure drop as the objective.

Rocha et al. (2012) studied the heat transfer between a pipe assembly and the soil during the annular temperature cycle. They used constructal design to find the flow structure that increased the heat transfer. They found that the optimal shapes change gradually from slender to square as the volume fraction occupied by the flow assembly increases. They also found that the heat transfer performance increases as the depth of the structure decreases but the depth has a negligible

effect on the shape of the structure. The performance also increases as the configuration of the ground volume and the buried structure evolves to the most slender shape possible.

In sum, the constructal law originated from the design of porous and complex flow structures, and now unites engineering, physics, biology, and social organization (Poirier 2003; Rosa et al. 2004; Reis 2006; Bejan and Lorente 2006, 2010, 2011, 2013). Constructal law books for the general public were published by Bejan and Zane (2012) and Bejan (2016). The use of this law is generating new theories in domains such as the design of the arterial tree (Silva and Reis 2014), the design of the termite ant mound (Kasimova et al. 2014), the design of brain vascularization and oxygenation (Hadjistassou et al. 2015), self-heating and self-cooling (Lee et al. 2013), multilayer insulation (Kang et al. 2013a, b, c), and the design of the ecohydrological flow architecture in the subsurface (Band et al. 2014).

4.19 Constructal Multiscale Flow Structures: Vascular Design

The tree-shaped flow structures of Sect. 4.18 are examples of "designed" porous structures with multiple length scales, which are organized hierarchically and distributed nonuniformly. These advances are reviewed in Bejan and Lorente (2008). Another class of designed porous media stems from an early result of constructal theory: the prediction of optimal spacings for the internal flow structure of volumes that must transfer heat and mass to the maximum (Bejan 2000; Sect. 4.15). Optimal spacings have been determined for several configurations, for example, arrays of parallel plates (e.g., Fig. 4.20). In each configuration, the reported optimal spacing is a single value, that is, a *single length scale* that is distributed uniformly through the available volume.

Is the stack of Fig. 4.20 the best way to pack heat transfer into a fixed volume? It is, but only when a single length scale is to be used, that is, if the structure is to be *uniform*. The structure of Fig. 4.20 is uniform, because it does not change from $x = 0$ to $x = L_0$. At the most, the geometries of single-spacing structures vary periodically, as in the case of arrays of cylinders and staggered plates.

Bejan and Fautrelle (2003) showed that the structure of Fig. 4.20 can be improved if more length scales ($D_0, D_1, D_2,...$) are available. The technique consists of placing more heat transfer in regions of the volume HL_0 where the boundary layers are thinner. Those regions are situated immediately downstream of the entrance plane $x = 0$. Regions that do not work in a heat transfer sense either must be put to work or eliminated. In Fig. 4.20, the wedges of fluid contained between the tips of opposing boundary layers are not involved in transferring heat. They can be involved if heat-generating blades of shorter lengths (L_1) are installed on their planes of symmetry. This new design is shown in Fig. 4.21.

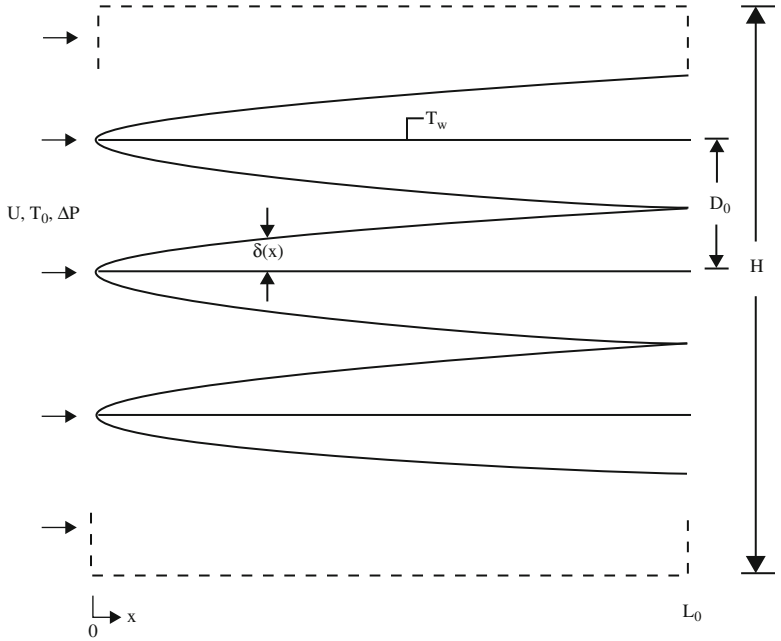

Fig. 4.20 Optimal package of parallel plates with one spacing (Bejan and Fautrelle 2003)

Each new L_1 blade is coated by Blasius boundary layers with the thickness $\delta(x) \cong 5x(Ux/\nu)^{-1/2}$. Because δ increases as $x^{1/2}$, the boundary layers of the L_1 blade merge with the boundary layers of the L_0 blades at a downstream position that is approximately equal to $L_0/4$. The approximation is due to the assumption that the presence of the L_1 boundary layers does not significantly affect the downstream development ($x > L_0/4$) of the L_0 boundary layers. This assumption is made for the sake of simplicity. The order-of-magnitude correctness of this assumption comes from geometry: the edges of the L_1 and L_0 boundary layers must intersect at a distance of order

$$L_1 \cong \frac{1}{4} L_0. \tag{4.166}$$

Note that by choosing L_1 such that the boundary layers that coat the L_1 blade merge with surrounding boundary layers at the downstream end of the L_1 blade, we once more invoke the maximum packing principle of constructal theory. We are being consistent as constructal designers, and because of this every structure with merging boundary layers will be optimal, no matter how complicated.

The wedges of isothermal fluid (T_0) remaining between adjacent L_0 and L_1 blades can be populated with a new generation of even shorter blades, $L_2 \cong L_1/4$. Two such blades are shown in the upper-left corner of Fig. 4.21. The length scales

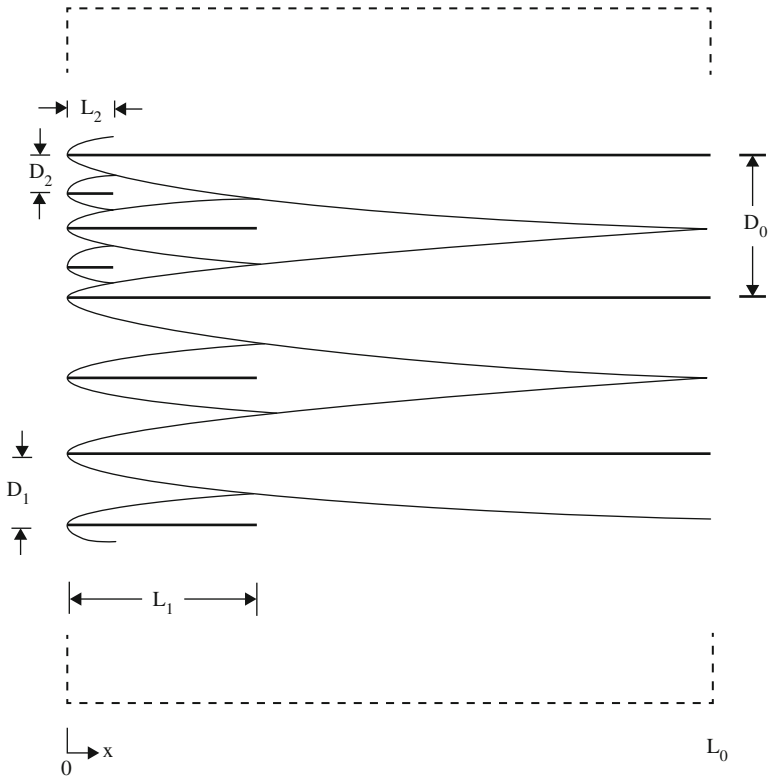

Fig. 4.21 Optimal multiscale package of parallel plates (Bejan and Fautrelle 2003)

become smaller (L_0, L_1, L_2), but the shape of the boundary layer region is the same for all the blades, because the blades are all swept by the same flow (U). The merging and expiring boundary layers are arranged according to the algorithm

$$L_i \cong \frac{1}{4} L_{i-1}, \quad D_i \cong \frac{1}{2} D_{i-1} \quad (i = 1, 2, ..., m), \tag{4.167}$$

where we show that m is finite, not infinite. In other words, as in all the constructal tree structures, the image generated by the algorithm is not a fractal [cf. Bejan (1997c, p. 765)]. The sequence of decreasing length scales is finite, and the smallest size (D_m, L_m) is known, as shown in Bejan and Fautrelle (2003) and Bejan et al. (2004). The global thermal conductance of the multiscale package is

$$\frac{q'}{k\Delta T} \cong 0.36 \frac{H}{L_0} \mathrm{Be}^{1/2} \left(1 + \frac{m}{2}\right)^{1/2} \tag{4.168}$$

where q' is the total heat transfer rate installed in the package (W/m, per unit length in the direction perpendicular to Fig. 4.21), k is the fluid thermal conductivity, and

ΔT is the temperature difference between the plates (assumed isothermal) and the fluid inlet. The dimensionless pressure and difference is

$$\mathrm{Be} = \frac{\Delta P L_0^2}{\mu \alpha}, \tag{4.169}$$

where μ and α are the fluid viscosity and thermal diffusivity.

Bejan and Fautrelle (2003) also showed that the optimized complexity increases with the imposed pressure difference (Be),

$$2^m \left(1 + \frac{m}{2}\right)^{1/4} \cong 0.17\,\mathrm{Be}^{1/4}. \tag{4.170}$$

As Be increases, the multiscale structure becomes more complex *and* finer. The monotonic effect of m is accompanied by diminishing returns: each smaller length scale (m) contributes to global performance less than the preceding length scale ($m - 1$). The validity of the novel design concept sketched in Fig. 4.21 was demonstrated through direct numerical simulations and optimization for multiscale parallel plates (Bello-Ochende and Bejan 2004) and multiscale parallel cylinders in cross flow (Bello-Ochende and Bejan 2005a). A related natural convection situation was treated by Bello-Ochende and Bejan (2005b).

Forced convection was used in Bejan and Fautrelle (2003) only for illustration, that is, as a language in which to describe the new concept. A completely analogous multiscale structure can be deduced for laminar natural convection. The complete analogy that exists between optimal spacings in forced and natural convection was described by Petrescu (1994). In brief, if the structure of Fig. 4.20 is rotated by 90° counterclockwise and if the flow is driven upward by the buoyancy effect, then the role of the overall pressure difference ΔP is played by the difference between two hydrostatic pressure heads, one for the fluid column of height L_0 and temperature T_0, and the other for the L_0 fluid column of temperature T_w. If the Boussinesq approximation applies, the effective ΔP due to buoyancy is

$$\Delta P = \rho g \beta \Delta T L_0, \tag{4.171}$$

where β is the coefficient of volumetric thermal expansion and g is the gravitational acceleration aligned vertically downward (against x in Fig. 4.20). By substituting the ΔP expression (4.171) into the Be definition (4.169) we find that the dimensionless group that replaces Be in natural convection is the Rayleigh number $\mathrm{Ra} = g\beta\Delta T L_0^3/\alpha v$ Other than the Be → Ra transformation, all the features that are due to the generation of multiscale blade structure for natural convection should mirror, at least qualitatively, the features described for forced convection in this section. The validity of the constructal multiscale concept for volumes packed with natural convection is demonstrated numerically in da Silva and Bejan (2005).

The hierarchical multiscale flow architecture constructed in this section is a theoretical comment on fractal geometry. Fractal structures are generated by

assuming (postulating) certain algorithms. In much of the current fractal literature, the algorithms are selected such that the resulting structures resemble flow structures observed in nature. For this reason, fractal geometry is descriptive, not predictive (Bejan 1997c; Bradshaw 2001). Fractal geometry is not a theory (Bejan and Zane 2012).

The more recent advances on designed porous media are being dedicated to the development of vascularized materials with new functionalities distributed throughout the volume: self-healing, self-cooling, mechanical strength, etc. This movement is reviewed in Bejan and Lorente (2006, 2008). Chief examples are the vascular design of solid plates permeated by fluids that provide self-healing (the fusing of internal fissures) and the volumetric cooling of plates subjected to intense heating under steady and unsteady conditions (Lorente and Bejan 2006, 2009a, b; Kim et al. 2006, 2009b; Zhang et al. 2009a, b, c; Combelles et al. 2009, 2012; Ordonez et al. 2003; Lee et al. 2008a, b, 2009a, b, c; Zeng et al. 2010; Cho et al. 2010a,b; Xu et al. 2008a, b; Wang et al. 2006, 2007c, 2009a, b; Moreno and Tao 2006; Rocha et al. 2009; Revellin et al. 2009; Kim et al. 2006, 2007, 2008d, 2009a, b). Vascular designs that provide both cooling and mechanical strength were developed by Wang et al. (2010c), Cetkin et al. (2011a, b), Miguel (2015, 2016), and Yenigun and Cetkin (2016).

4.20 Optimal Spacings for Plates Separated by Porous Structures

Taking the concept of Fig. 4.20 even closer to traditional porous media, consider the optimization of spacings between plates that sandwich a porous medium (Bejan 2004a). For example, the channels may be occupied by a metallic foam such that the saturated porous medium has a thermal conductivity (k_m) and a thermal diffusivity (α_m) that are much higher than their pure fluid properties (k_f, α_f). We consider both natural convection and forced convection with Boussinesq incompressible fluid and assume that the structures are fine enough that Darcy flow prevails in all cases. The analysis is another application of the intersection of asymptotes method (Lewins 2003).

The natural convection configuration is shown in Fig. 4.22. This time each D-thin space is filled with the assumed fluid-saturated porous structure. The width in the direction perpendicular to Fig. 4.22 is W. The effective pressure difference that drives the flow is due to buoyancy:

$$\Delta P = \rho H g \beta (T_w - T_0). \tag{4.172}$$

This ΔP estimate is valid in the limit where the spacing D is sufficiently small so that the temperature in the channel porous medium is essentially the same as the plate temperature T_w. In this limit, the heat current extracted by the flow from the $H \times L$ volume is $q = \dot{m} c_P (T_w - T_0)$, with $\dot{m} = \rho U L W$ and Darcy's law,

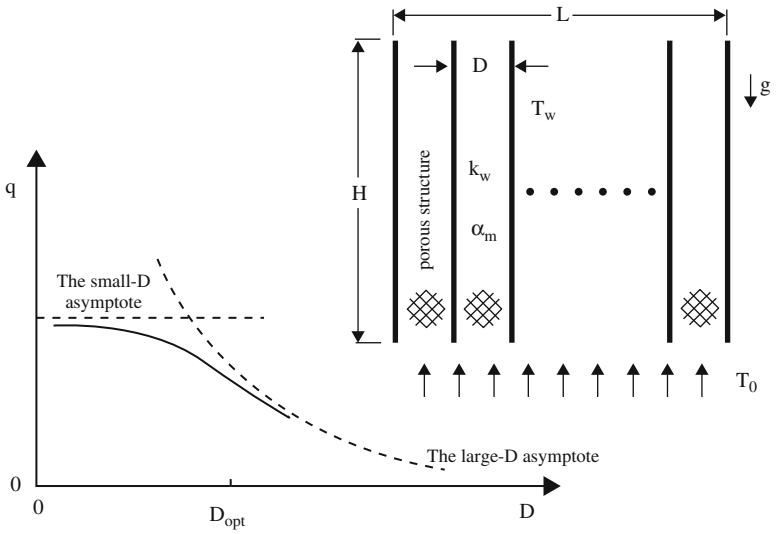

Fig. 4.22 Volume filled with vertical heat-generating plates separated by a fluid-saturated porous medium, and the effect of the channel spacing on the global thermal conductance (Bejan 2004a)

$U = K\Delta P/\mu H$, where K is the permeability of the structure. In conclusion, the total heat transfer rate in the small-D limit is independent of the spacing D,

$$q = \rho c_P (T_w - T_0) LW\,(K\,\Delta P)/\mu H. \tag{4.173}$$

In the opposite limit, D is large so that the natural convection boundary layers that line the H-tall plates are distinct. The heat transfer rate from one boundary layer is $\bar{h}HW(T_w - T_0)$, where $\bar{h}H/k = 0.888\mathrm{Ra}_H^{-1/2}$, and $\mathrm{Ra_H}$ is the Rayleigh number for Darcy flow, $\mathrm{Ra}_H = Kg\beta H(T_w - T_0)/\alpha_m\nu$. The number of boundary layers in the $H \times L$ volume is $2L/D$. In conclusion, the total heat transfer rate decreases as D increases,

$$q = 1.78\,(L/D)Wk\,(T_w - T_0)\mathrm{Ra}_H^{1/2}. \tag{4.174}$$

For maximal thermal conductance $q/(T_w - T_0)$, the spacing D must be smaller than the estimate obtained by intersecting asymptotes (4.173) and (4.174), cf. Bejan (2013):

$$D_{opt}/H \leq 1.78\,\mathrm{Ra}_H^{-1/2}, \tag{4.175}$$

The simplest design that has the highest possible conductance is the design with the fewest plates (i.e., the one with the largest D_{opt}); hence $D_{opt}/H \cong 1.78\,\mathrm{Ra}_H^{-1/2}$ for the recommended design. Contrary to Fig. 4.22, however, q does not remain

constant if D decreases indefinitely. There exists a small enough D below which the passages are so tight (tighter than the pores) that the flow is snuffed out. An estimate for how large D should be so that Eq. (4.175) is valid is obtained by requiring that the D_{opt} value for natural convection when the channels are filled only with fluid, $D_{\text{opt}}/H \cong 2.3\ [g\beta H^3(T_w - T_0)/\alpha_f \nu]^{-1/4}$ must be smaller than the D_{opt} value of Eq. (4.163). We find that this is true when

$$\frac{H^2}{K}\,\frac{\alpha}{\alpha_{\text{f}}} > \text{Ra}_H, \tag{4.176}$$

in which, normally, $\alpha/\alpha_{\text{f}} \gg 1$ and $H^2/K \gg 1$.

The forced convection configuration can be optimized similarly (Bejan 2004a). The flow is driven by the imposed ΔP through parallel-plate channels of length L and width W. It is found that the forced convection asymptotes have the same behavior as in Fig. 4.22. The highest conductance occurs to the left of the intersection of the two asymptotes, when

$$D_{\text{opt}}/L \lesssim 2.26\,\text{Be}_p^{-1/2} \tag{4.177}$$

and where Be_p is the porous medium Bejan number, $\text{Be}_p = (\Delta P\, K)/\mu\alpha_{\text{m}}$. This forced convection optimization is valid when the D_{opt} estimate for the channel with pure fluid is smaller than the D_{opt} value provided by Eq. (4.177) when

$$\frac{L^2}{K}\,\frac{\alpha}{\alpha_{\text{f}}} > \text{Be}_p. \tag{4.178}$$

In summary, Eqs. (4.175) and (4.177) provide estimates for the optimal spacings when the channels between heat-generating plates are filled with a fluid-saturated porous structure. The relevant dimensionless groups are Ra_H, Be_p, K/H^2, K/L^2, and $\alpha_{\text{m}}/\alpha_{\text{f}}$. The symmetry between Eqs. (4.175) and (4.177) and between Eqs. (4.176) and (4.178) reinforces Petrescu's (1994) argument that the role of the Bejan number in forced convection is analogous to that of the Rayleigh number in natural convection.

Optimal spacings are also applied in Sect. 3.7.

These results are most fundamental and are based on a simple model and a simple analysis: Darcy flow and the intersection of asymptotes method. The same idea of geometry optimization deserves to be pursued in future studies of "designed porous media," based on more refined models and more accurate methods of flow simulation.